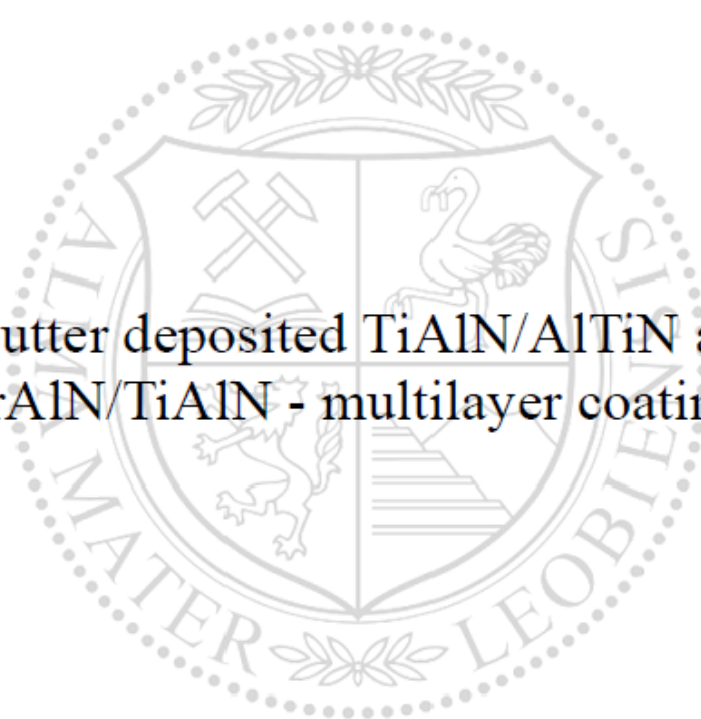




Chair of Functional Materials and Materials Systems

Master's Thesis



Sputter deposited TiAlN/AlTiN and
CrAlN/TiAlN - multilayer coatings

Stefan Blumauer, BSc

May 2021



MONTANUNIVERSITÄT LEOBEN

www.unileoben.ac.at

EIDESSTÄTTLICHE ERKLÄRUNG

Ich erkläre an Eides statt, dass ich diese Arbeit selbständig verfasst, andere als die angegebenen Quellen und Hilfsmittel nicht benutzt, und mich auch sonst keiner unerlaubten Hilfsmittel bedient habe.

Ich erkläre, dass ich die Richtlinien des Senats der Montanuniversität Leoben zu "Gute wissenschaftliche Praxis" gelesen, verstanden und befolgt habe.

Weiters erkläre ich, dass die elektronische und gedruckte Version der eingereichten wissenschaftlichen Abschlussarbeit formal und inhaltlich identisch sind.

Datum 03.05.2021

Unterschrift Verfasser/in
Stefan Blumauer

Affidavit:

I declare in lieu of ought, that I wrote this thesis and performed the associated research myself, using only literature cited in this work.

Leoben, May 2021

Stefan Blumauer

Acknowledgments

I am very grateful to my mentor Dipl.-Ing. Helene Waldl, for her patience and support while supervising me at writing this thesis. She was always there to help me solve problems and answer questions quickly. I would also like to thank her for her helpfulness, the many ideas and tips she gave me as well as time-consuming discussions we had.

I would also like to thank Dipl.-Ing. Dr. Nina Schalk, head of the Christian Doppler Laboratory for Advanced Coating Cutting Tools, Dipl.-Ing. Dr. Michael Tkadletz and Dipl.-Ing. Dr. Christina Kainz, for the confidence they have had in welcoming me into their group.

A big thank you goes to Univ.-Prof. Dipl.-Ing. Dr. Christian Mitterer, head of the Chair of Functional Materials and Materials Systems, for the opportunity to write this thesis at his chair.

Furthermore, I would like to acknowledge Sabrina Hirn, Mag. Velislava Terziyska and Karl-Heinz Pichler for the friendly and helpful support during deposition of the coatings for my master thesis and the many nice conversations we had.

I am grateful to Assoz. Univ.-Prof. Dr Rostislav Daniel and Walter Baumegger for their help with “Debbie” whenever I needed it.

In addition, I would like to thank the all members of the Thin-Film Group for helping me in any case and for the nice discussions during the breaks.

My special thanks go to the dear friends in my life. They enrich my life at so many levels. Without you I would have missed many experiences, memories and funny moments. I am glad to have you by my side.

Finally, I would like to thank my family, especially my parents. They have always been by my side and have made my studies in Leoben possible. They have always encouraged me, even in difficult moments.

Table of Contents

1	Introduction	1
2	Theoretical Background	3
2.1	Physical Vapor Deposition	3
2.1.1	Magnetron Sputtering	3
2.1.2	Structure Zone Models	5
2.2	Ti-Al-N System	6
2.2.1	Microstructure	7
2.2.2	Mechanical Properties and Thermal Stability	8
2.3	Cr-Al-N System	11
2.3.1	Microstructure	12
2.3.2	Mechanical Properties and Thermal Stability	12
2.4	Multilayer Coatings	14
3	Experimental Methods	18
3.1	Coating Deposition	18
3.1.1	Single Layer Coatings	19
3.1.2	Multilayer Coatings	20
3.2	Coating Characterization	20
3.2.1	Coating Thickness	20
3.2.2	Layer Architecture	20
3.2.3	Chemical Composition	21
3.2.4	Microstructure	21
3.2.5	Hardness and Young's modulus	21
4	Results and Discussion	22
4.1	Single Layer Coatings	22
4.1.1	Coating Thickness	22
4.1.2	Chemical Composition	23
4.1.3	Microstructure	23
4.1.4	Mechanical Properties	26
4.2	Multilayer Coatings	27
4.2.1	Coating Thickness	27
4.2.2	Microstructure	28
4.2.3	Chemical Composition	33
4.2.4	Mechanical Properties	34
5	Summary and Conclusion	36
	References	38

1 Introduction

In the last decades, there were a lot of research activities on hard protective coatings for forming and machining applications, to improve their performance and therefore the service lifetime [1, 2]. Hard coatings with a thickness of a few microns exhibit attractive mechanical and chemical properties such as high hardness, thermal stability and chemical inertness, as well as wear, oxidation and corrosion resistance [3, 4]. Physical vapour deposition techniques, like for example magnetron sputtering or cathodic arc evaporation, can be used to synthesize a variety of different coating materials [5, 6]. A coating system, which has been shown to improve the cutting performance and lifetime of cutting tools significantly, is $Ti_{1-x}Al_xN$ [7, 8]. $Ti_{1-x}Al_xN$ represents a metastable solid solution with a face-centred cubic (fcc) based structure up to an Al metal fraction x of ~ 0.65 . The Al addition results in improved properties at elevated temperatures [3, 4]. At higher Al contents, the formation of wurtzite (w) AlN sets in, which reduces the hardness [7, 8]. At ~ 900 °C, $Ti_{1-x}Al_xN$ decomposes into fcc-TiN and fcc-AlN rich domains, which is accompanied by age hardening. Upon further increasing the temperature, the metastable fcc-AlN transforms into the stable w-AlN. This results in a deterioration of the mechanical properties, especially the hardness [4, 9]. An alternative coating system with similar behaviour and properties is $Cr_{1-x}Al_xN$. As $Ti_{1-x}Al_xN$, $Cr_{1-x}Al_xN$ is used as a hard coating material for machining tools to improve their lifetime and performance. Compared to $Ti_{1-x}Al_xN$, $Cr_{1-x}Al_xN$ exhibits a better oxidation and corrosion resistance at elevated temperatures [4, 10]. Increasing the Al content within the fcc-regime has a positive influence on the mechanical properties and thermal stability of the deposited coating [2, 4].

In addition to single layer coatings, it is also possible to deposit multilayer coatings [3, 11]. By varying the composition and thickness of the individual sublayers, the properties of multilayer coatings can be strongly influenced. Thus, the application of a multilayered coating architecture enables an improvement of the mechanical properties and thermal stability compared to single layers [12].

The aim of this thesis is the investigation of multilayer coatings with different Al contents and variable sublayer thicknesses in the system TiAlN/AlTiN and CrAlN/TiAlN. The multilayer architecture was used to achieve a higher overall Al content in the coatings in comparison to the single layered coatings. Nine TiAlN/AlTiN and CrAlN/TiAlN coatings with three defined sublayer thicknesses as well as the corresponding four single layers with different Al/Ti ratios

(50/50, 70/30 and 80/20) and an Al/Cr ratio of 85/15 were deposited by unbalanced magnetron sputter deposition. Throughout the present thesis, TiAlN denotes Ti rich and AlTiN Al rich layers. Subsequent crystallographic, microscopic and mechanical investigations allowed to understand the influence of the layer architecture on the microstructure and properties of the coatings.

2 Theoretical Background

2.1 Physical Vapor Deposition

Physical vapor deposition (PVD) techniques are used to coat for example cutting inserts or electronic and optical devices with a coating thickness up to several μm [5, 13]. The PVD process consists of three main steps: (i) a solid material is vaporized, (ii) the vapor is transported from the target to the substrate and (iii) the vapor condenses on a surface, where nucleation and film growth occur [2, 14]. The target consists of the solid material which is evaporated or sputtered. An advantage of the PVD process is that almost all kinds of materials can be used as target (e.g. metals, alloys, compounds) and substrates (e.g. metals, plastics, glass), compared to chemical vapor deposition (CVD). In contrast to CVD where thermal activation is required, PVD allows low deposition temperatures [5, 15]. One disadvantage of PVD processes is that they are line-of-sight processes, which means that only the parts of the substrate, which are directly facing the target, are coated homogeneously. PVD processes can be basically classified into sputter deposition and evaporation. The sputter deposition process is explained in more detail below, since this process was used for the deposition of the coatings in the present work [3].

2.1.1 Magnetron Sputtering

The sputtering process is based on the erosion of atoms from the target surface by ion bombardment. Usually, the noble (i.e. non-reactive) gas Ar is used as ionized gas, which is also referred to as process gas. To initiate the sputter process, the vacuum chamber is filled with Ar gas and an electric field between the target, forming the cathode, and the grounded vacuum chamber, the anode, is applied. The electric field is generated by an external power supply [3, 13]. The Ar atoms are ionized through inelastic collision of neutral atoms and accelerated electrons, generated by a glow discharge, creating the so-called plasma. The ionized atoms are accelerated towards the negatively charged target, where the target atoms are vaporized by energy and momentum transfer. The sputtering yield is the number of target atoms ejected per incident ion [16]. This released vapor typically consists mainly of neutral atoms. The coating forms through condensation of these target atoms on the grounded or biased substrate [1, 3, 17]. A negative bias voltage on the substrate increases the potential between plasma and substrate surface. Thus, the ion bombardment on the substrate is

enhanced, resulting in local heating of the substrate, the so called atomic scale heating and consequently in an enhanced mobility of the condensed atoms leading to improved coating properties [3, 5].

The deposition rate can be increased with the use of a magnetron. There, permanent magnets are arranged behind the target in such a way that the magnetic field is parallel to the target surface and therefore the electrons are concentrated near the target. This principle is based on the Lorentz force. As shown in **Figure 1**, the magnet generates a so-called electron trap: the free electrons are forced to move in a cycloid path near the target surface, which increases the number of ionization events and consequently results in an enhanced sputter rate [3, 5, 18]. Depending on the configuration of the magnetic field lines, magnetron sputtering can be divided in balanced or unbalanced magnetron sputtering. In the balanced configuration, all magnetic field lines loop between the two magnets and the plasma is primarily confined near the target. In case of unbalanced magnetron sputtering, several of the magnetic field lines are open towards the substrate (**Figure 1**), as one magnet is stronger than the other [3, 18]. With the unbalanced magnetron arrangement, a higher deposition rate is achieved due to the higher target current. In addition, the ionization rate near the substrate increases, resulting in enhanced ion bombardment of the growing film and thus, in improved coating properties [18]. It is possible to use reactive gases in the deposition process, which is referred to as reactive sputtering [1, 3]. The reactive gas, for example N_2 , CH_4 or O_2 , reacts with the target atoms and consequently forms the desired compound. The reaction can also occur on the target surface, which results in target poisoning and subsequently leads to a lower deposition rate. Therefore, the adsorption of the reactive gas and reaction on the substrate is to be favoured [3, 13].

Sputtering can be done in three different modes: direct-current (DC), pulsed DC and radio-frequency (RF). The DC-mode is often used due to the cheap power supply and the easy process control. However, there are two main disadvantages of this technique: (i) the low deposition rate in reactive sputtering due to target poisoning and (ii) the restriction to conductive targets. Using pulsed DC or RF allows to overcome these problems through permanently discharging the charged target surface. In both cases, the electrons and ions can still move between the electrodes [3, 5, 14]. **Figure 1** shows a schematic of a DC unbalanced magnetron sputtering system. This setup is similar to the one used in this thesis.

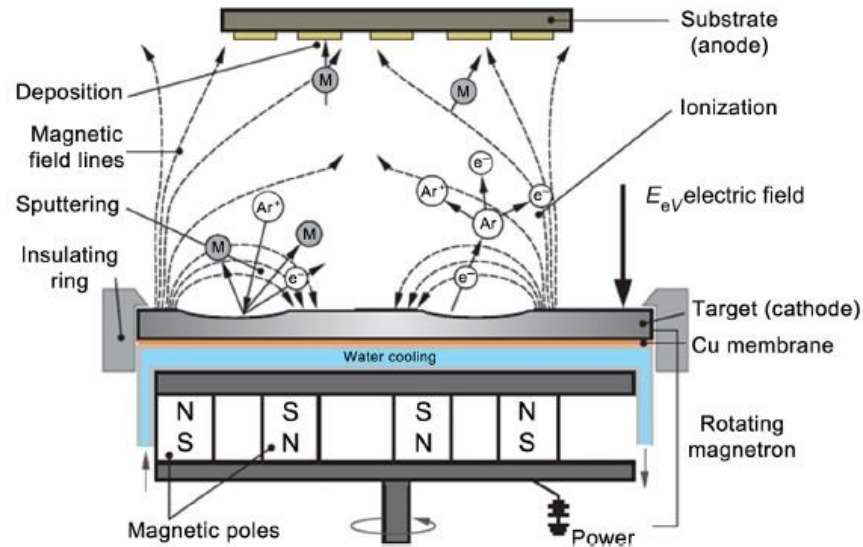


Figure 1: Schematic of a DC unbalanced magnetron sputtering system [3].

The main advantage of sputtering compared to arc evaporation is the absence of droplets, representing molten target material and being characteristic for cathodic arc evaporation, which are incorporated into the coating. Therefore, sputter deposited coatings have a smooth homogeneous structure. However, in comparison to arc evaporation, the deposition rate and the ionization rate of the vaporized species are significantly lower in sputtering [3, 5].

2.1.2 Structure Zone Models

The microstructure of the coating is influenced by the diffusion of adatoms. The growth process of the coating depends for example on the deposition rate, gas pressure, bias voltage and substrate temperature [13]. Thus, it is crucial to understand the relationship between microstructure and deposition parameters. To illustrate these relations, structure zone models (SZM) have been developed [13]. There are SZMs proposed by Movchan and Demchishin [19], Thornton [20], Messier *et al.* [21] and Anders [22].

Figure 2 illustrates the SZM by Thornton, which is used to describe the observed microstructures of sputter deposited coatings. Thornton reports four different structural zones as a function of the homologous temperature T/T_m and Ar pressure. T is the substrate temperature and T_m is the melting temperature of the coating material. In zone 1, the temperature is low, thus the mobility of the adatoms is limited. The coating is porous with columnar grains. In the transition zone (zone T), competitive growth of differently oriented crystals develops and the coating exhibits fibrous grains. Furthermore, the coating is denser compared to zone 1. In zone 2, the effect of grain boundary migration becomes relevant. Here,

surface diffusion is the predominating process and the coating microstructure is characterized by columnar grains. Zone 3, where the homologous temperature is higher than 0.5, is dominated by dense equiaxed grains and a smooth surface. In this zone, the temperature is high enough for bulk diffusion, which results in recrystallization [20].

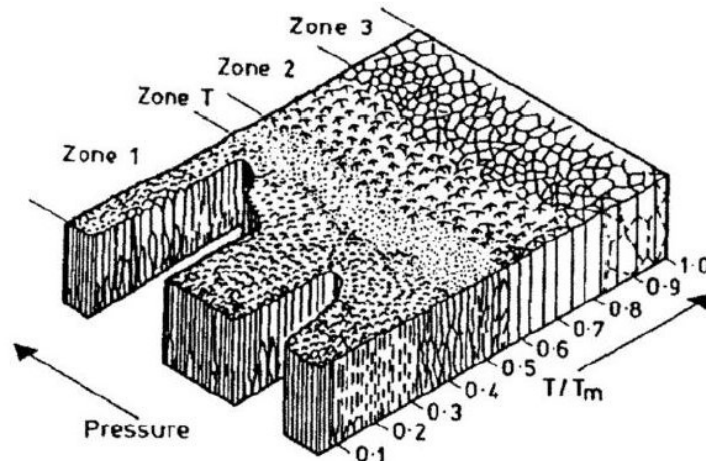


Figure 2: SZM by Thornton for magnetron sputter deposited films [20].

2.2 Ti-Al-N System

With the exception of diamond, all hard materials exhibit a combination of metallic, covalent or ionic bonding [23]. The dominating bonding type defines the thermal stability and mechanical properties of a material, as can be seen in **Figure 3**. Ideal hard coatings should exhibit high hardness, good adhesion to the substrate and high chemical stability. In order to enable a combination of these properties, hard materials in the middle of the bonding triangle, such as TiN or TiAlN, are frequently used [24].

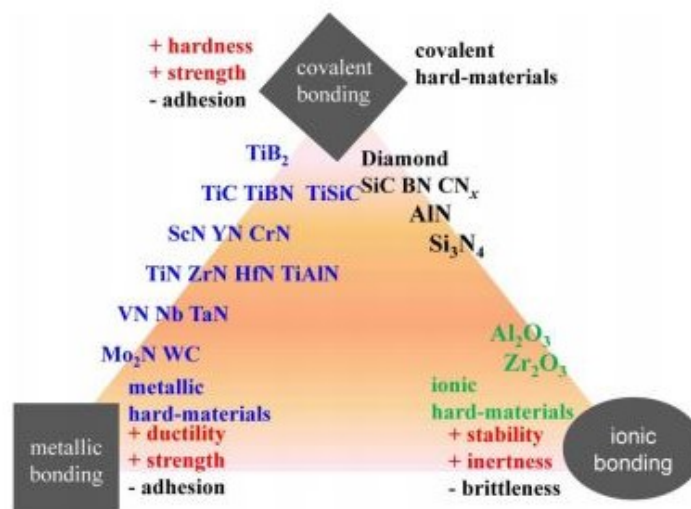


Figure 3: Classification of hard materials [25].

TiN coatings have a wide range of technical applications, for example as diffusion barriers, gate material and protective coatings. Owing to its golden-yellow colour, TiN is also used for decorative coatings [3, 4]. The equilibrium phase diagram of Ti-N is shown in **Figure 4** [2]. TiN has a fcc NaCl structure with a nitrogen content in the range of 37.5 – 50 at.% [2, 26]. TiN exhibits a good thermal stability and corrosion resistance and a high hardness up to 32 GPa when synthesized by magnetron sputtering. However, at temperatures exceeding ~550 °C, the hardness and oxidation resistance are poor [2, 3].

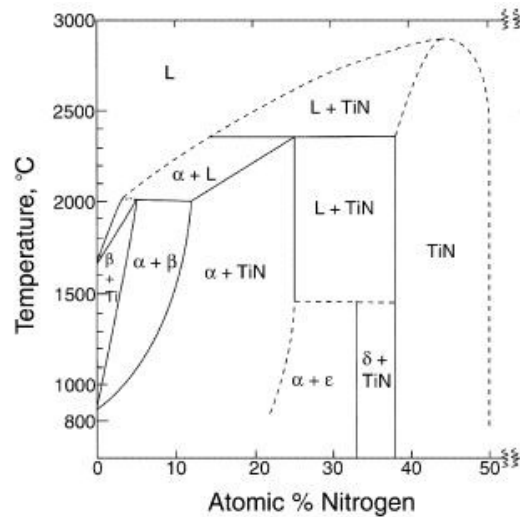


Figure 4: Equilibrium phase diagram of Ti-N binary system [2].

To improve the cutting performance, all relevant wear mechanisms have to be considered. To overcome the shortcomings of TiN at elevated temperatures, it is replaced by ternary compounds in severe applications. A commonly used substitute for TiN in the machining industry is TiAlN [8].

2.2.1 Microstructure

The formation of fcc-Ti_{1-x}Al_xN is achieved through the substitution of Ti atoms by Al atoms until the maximum solubility of Al is reached. AlN has mainly covalent bonds in a hexagonal (hex) close packed (hcp) B4 ZnS-wurtzite-type structure [2]. Wurtzitic (w)-AlN and fcc-TiN have a low mutual solubility, as can be seen in **Figure 5a**. The use of PVD techniques, however, allows to synthesize the supersaturated solid solution Ti_{1-x}Al_xN, which is metastable [3, 4]. **Figure 5b** illustrates the metastable phase diagram of Ti_{1-x}Al_xN, where the two single phase regions for cubic and hex Ti_{1-x}Al_xN are separated by a two-phase region. In the two single phase regions, cubic and hex solid solutions can occur.

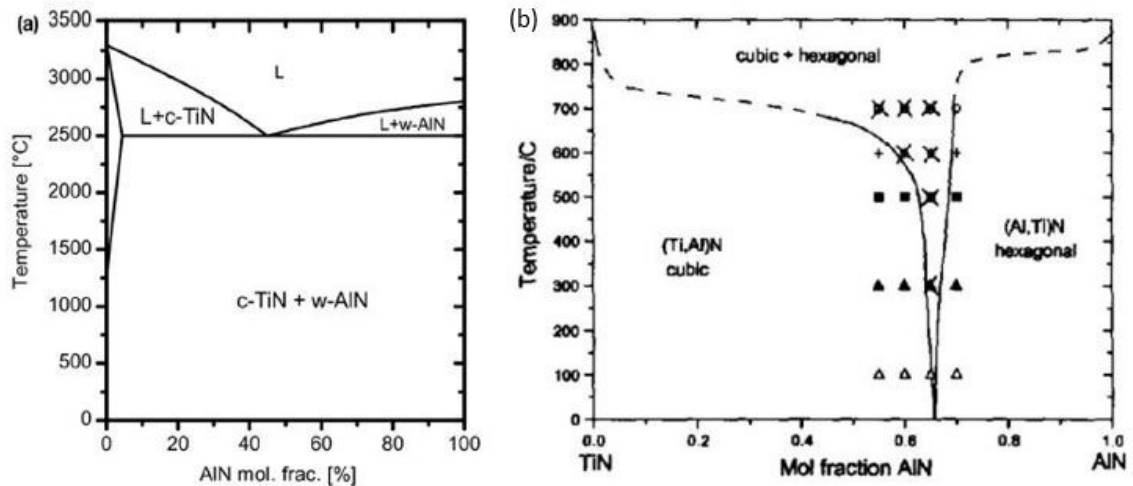


Figure 5: (a) Equilibrium phase diagram [4] and (b) modified metastable phase diagram of $Ti_{1-x}Al_xN$ [27].

$Ti_{1-x}Al_xN$ exhibits a single fcc-structure up to Al metal fractions of 0.4 – 0.7, the metastable solubility limit, followed by a mixed fcc and w-structure and a single-phase w-structure at high Al contents. This structural development is shown in **Figure 6** [2, 4, 28]. The solubility limit is affected by the deposition parameters. Since a higher Al content within the fcc-regime results in improved mechanical and thermal properties, a shift of the solubility limit to higher Al contents is favourable [29].

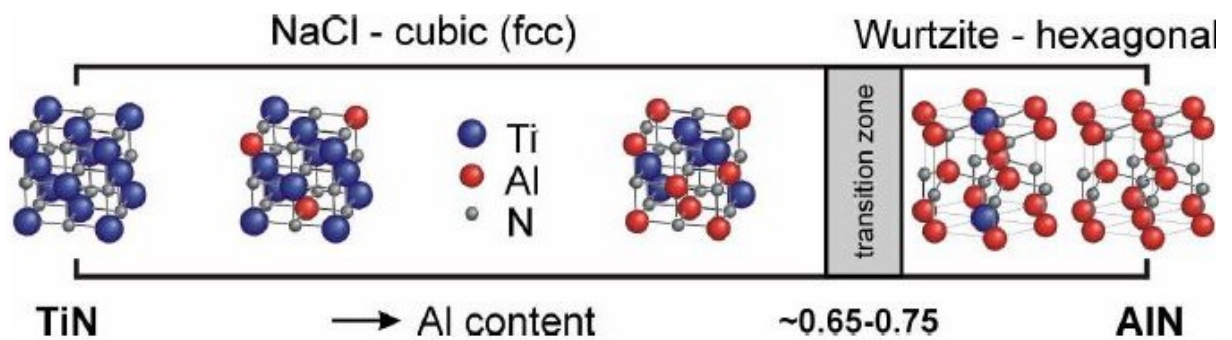


Figure 6: Structural development of $Ti_{1-x}Al_xN$ as a function of the Al content [30].

2.2.2 Mechanical Properties and Thermal Stability

In order for cutting tools to have a long lifetime and a good performance, a high hardness is required [7, 8]. The smaller atomic radius of the Al atoms compared to Ti results in a decreasing lattice parameter with increasing amount of Al in $Ti_{1-x}Al_xN$. The addition of Al to TiN causes a hardness increase due to solid solution hardening. Lattice distortion, stemming from the substitution of the atoms, makes plastic deformation more difficult owing to the limited dislocation movement through stress fields. Further, the finer grain size with higher Al

content also contributes to the hardness increase according to the Hall-Petch effect [31, 32]. As illustrated in **Figure 7a** and **b**, hardness and Young's modulus reach a maximum value when in the fcc-structure the highest Al content (~ 0.65) is reached [2, 27]. Upon further increasing the Al content, the hardness and Young's modulus decrease due to the formation of the w-structure.

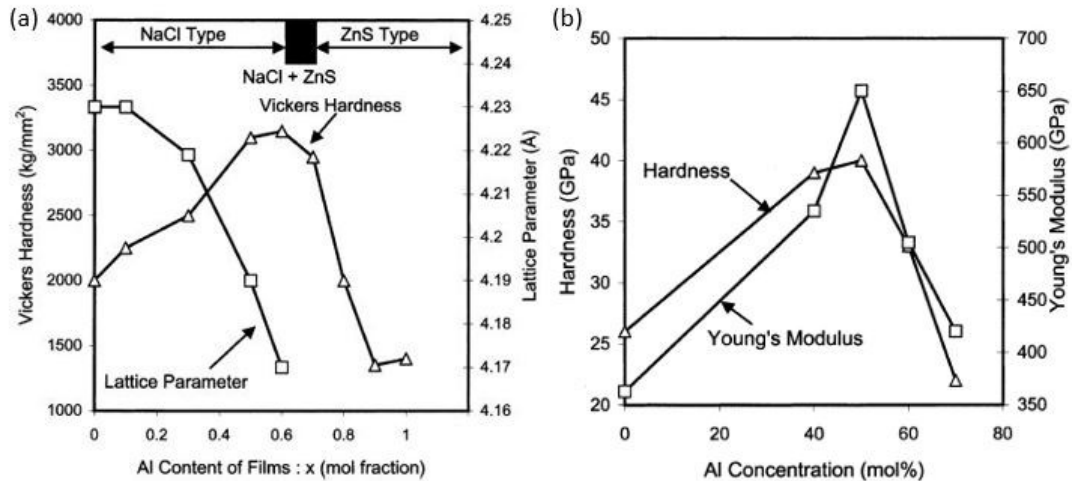


Figure 7: (a) Change in lattice parameter and microhardness as a function of the Al concentration of $Ti_{1-x}Al_xN$ coatings. (b) Hardness and Young's modulus as a function of the Al concentration in $Ti_{1-x}Al_xN$ coatings [2].

In addition to the composition dependent mechanical properties at room temperature, the evolution of the hardness of $Ti_{1-x}Al_xN$ at elevated temperature has been thoroughly investigated in literature [4, 27]. While for TiN a decrease in hardness at temperatures exceeding $400\text{ }^\circ\text{C}$ is observed [27], the hardness of $Ti_{1-x}Al_xN$ increases with increasing temperature until w-AlN is formed. The observed hardness increase is a result of age hardening caused by spinodal decomposition [4, 27]. **Figure 8** summarizes the whole sequence of microstructural development with increasing temperature. In the as-deposited state, $Ti_{1-x}Al_xN$ exhibits a homogeneous microstructure with minor chemical fluctuations. Due to spinodal decomposition at $\sim 800\text{-}1000\text{ }^\circ\text{C}$, fcc-TiN and fcc-AlN enriched domains with coherent interfaces are formed, resulting in significant strains due to a lattice mismatch between the coherent cubic domains, which prevents dislocation movement and thus results in age hardening [9].

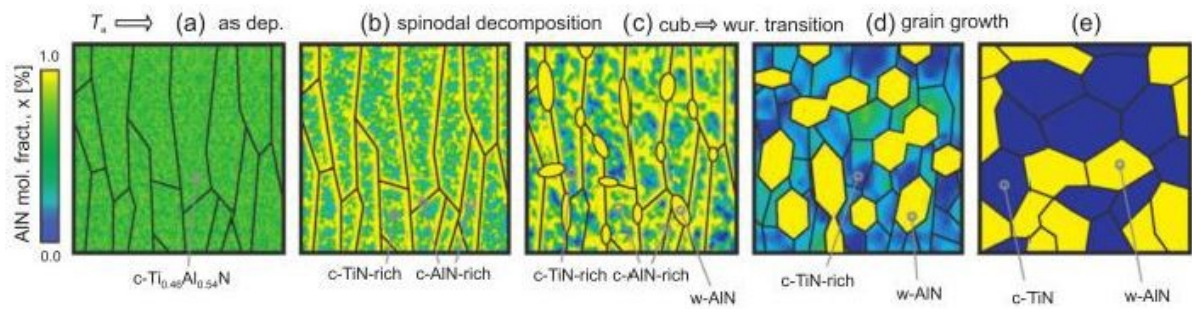


Figure 8: Schematic representation of the microstructural evolution of an fcc-Ti_{1-x}Al_xN coating. (a) As-deposited state with minor chemical fluctuations of the composition, (b) formation of fcc-AlN-rich and fcc-TiN-rich domains via spinodal decomposition, (c) ongoing decomposition and formation of w-AlN, (d) Al diffusion out of the fcc-TiN grains and growth of w-AlN, (e) grain growth of the dual phase structure [9].

Upon further increasing the temperature, the metastable fcc-AlN transforms into the stable w-AlN structure. With further increasing temperature, the grains grow and the grain boundary volume is reduced. The formation of w-AlN and the grain growth result in a deterioration of the mechanical properties, especially the hardness, as can be seen in **Figure 9** [27, 33]. The temperature, where the hardness peak occurs, depends on the Al content, since a high Al content is a driving force for decomposition. Thus, spinodal decomposition occurs at lower temperatures in coatings with higher Al contents [27]. This observation is corroborated by thermodynamic and *ab initio* calculations as well as by experimental studies [34, 35, 36].

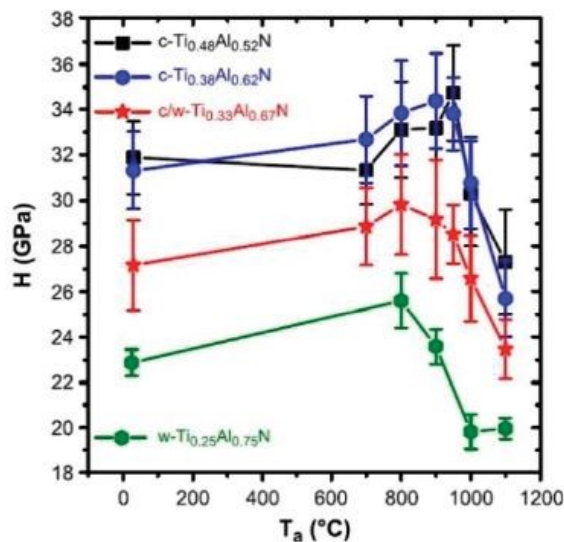


Figure 9: Evolution of hardness with annealing temperature for Ti_{1-x}Al_xN coatings with different Al contents [27].

The outstanding performance of Ti_{1-x}Al_xN coatings is also attributed to the oxidation resistance and the wear behaviour of this material. TiN oxidizes at approximately 550 – 600 °C, whereas Ti_{1-x}Al_xN coatings withstand temperatures as high as 800 °C without signs of oxidation. The

reason is the formation of a dual-phase oxide layer, consisting of a porous rutile (r)-TiO₂ layer with a dense α -Al₂O₃ protective layer on top, acting as diffusion barrier [2, 3, 27]. As shown in **Figure 10**, the oxidation behaviour depends on the oxidation temperature and the Al content in the coating. At higher Al contents, the oxidation resistance is improved significantly due to the presence of an amorphous Al₂O₃ film [2, 27]. For achieving a good oxidation resistance, the Al content should be close to the solubility limit [3].

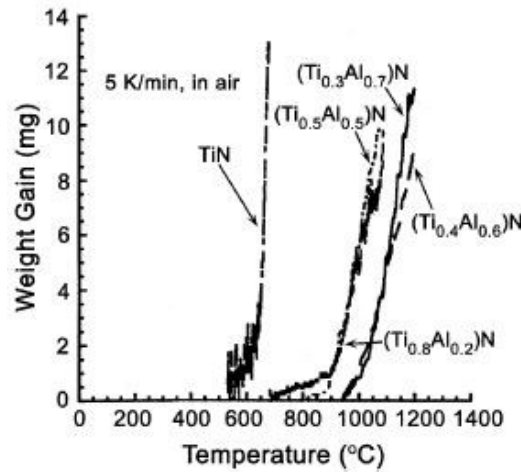


Figure 10: Oxidation curves of Ti_{1-x}Al_xN coatings with different Al contents as a function of temperature [2].

2.3 Cr-Al-N System

CrN exhibits excellent corrosion resistance, good wear properties and good adhesion [3, 10, 16]. Typical applications are protective layers, when the tool is subjected to tribological and corrosive loads [3]. CrN exhibits a high hardness and an oxidation resistance up to 700 °C. The sputtering yield is two to four times higher than for TiN, which enables high productivity and cost reduction [10, 16, 37]. CrN coatings typically exist in two possible modifications: CrN with an fcc-NaCl structure and Cr₂N with a hex structure. The obtained modification depends on the nitrogen flow rate and the temperature. As shown in **Figure 11**, CrN has a very narrow phase field in the range of 49.5 – 50 at.% nitrogen. The stability field of Cr₂N extends from 30.3 – 33.3 at.% nitrogen at room temperature [16]. To improve the mechanical properties, thermal stability and oxidation resistance, commonly Al is alloyed to the binary CrN system to form Cr_{1-x}Al_xN. Cr_{1-x}Al_xN is used as a hard coating material for machining tools to improve their lifetime and performance [4, 10].

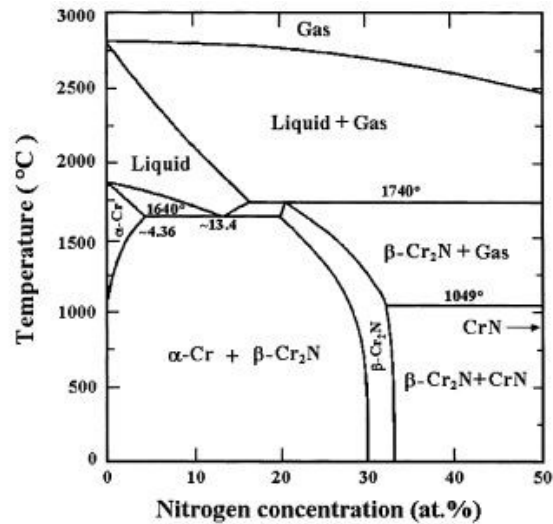


Figure 11: Equilibrium phase diagram of the Cr-N system [16].

2.3.1 Microstructure

Similar to w -AlN and fcc-TiN, w -AlN and fcc-CrN have a low mutual solubility [38]. $Cr_{1-x}Al_xN$ undergoes a similar evolution of the crystal structure like $Ti_{1-x}Al_xN$ as a function of the Al content. The Al atoms substitute for the Cr atoms until the maximum solubility of Al in fcc-CrN is reached. As shown in **Figure 12**, $Cr_{1-x}Al_xN$ exhibits at $x \sim 0.7$ a phase transformation from the NaCl type to the B4 w -type structure. Between an Al content of 0.7 – 0.77, the fcc- and the w -phases coexist in the coating [38].

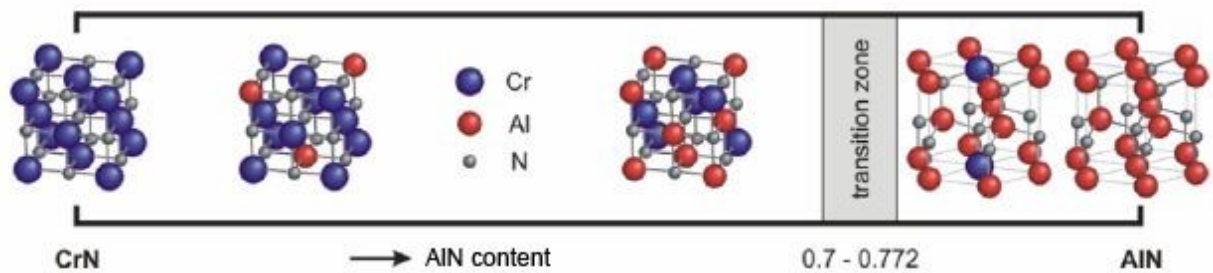


Figure 12: Evolution of the microstructure of $Cr_{1-x}Al_xN$ [38].

2.3.2 Mechanical Properties and Thermal Stability

Similar to $Ti_{1-x}Al_xN$, the substitution of Cr with Al atoms leads to a decrease of the lattice parameter of the fcc- $Cr_{1-x}Al_xN$ phase and the hardness increases due to solid solution hardening. Above the critical Al solubility, w -AlN starts to form, which leads to a drop of the hardness. **Figure 13** shows that the maximum hardness of 27 GPa for $Cr_{1-x}Al_xN$ is reached at an Al content of $x \sim 0.6$ [39].

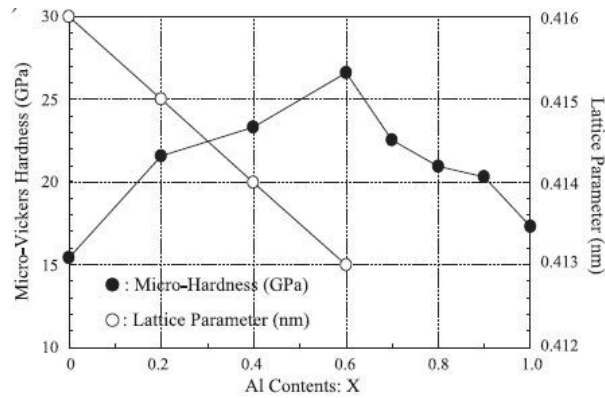


Figure 13: Evolution of lattice parameter and microhardness of $\text{Cr}_{1-x}\text{Al}_x\text{N}$ coatings with increasing Al content [39].

The Al content influences the onset of decomposition of $\text{Cr}_{1-x}\text{Al}_x\text{N}$ during annealing. With an Al content close to the solubility limit, the hardness increases slightly up to a temperature of 600 °C, as demonstrated in **Figure 14**. A further increase of the temperature to 725 °C results in a significant increase of the hardness due to the transformation and precipitation of an incoherent w-AlN phase from the fcc-AlN phase. The hardening effect continues as long as the additional phase is small in size and of only small volume fraction [4]. Age-hardening is caused by the formation of the w-AlN particles during the early stages of decomposition. With increasing content of the w-AlN phase, the hardness decreases rapidly [4].

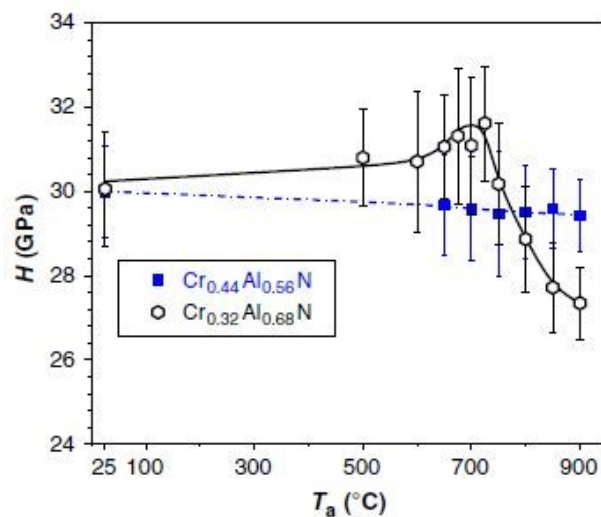


Figure 14: Evolution of hardness with increasing annealing temperature for $\text{Cr}_{1-x}\text{Al}_x\text{N}$ coatings with different Al content [4].

The initiation of the decomposition into the stable constituents fcc-CrN and w-AlN depends on the structure of the metastable $\text{Cr}_{1-x}\text{Al}_x\text{N}$ coating. **Figure 15a** shows the decomposition of metastable fcc- $\text{Cr}_{1-x}\text{Al}_x\text{N}$ coatings. Formation of the w-AlN phase sets in between 1000 and 1300 °C, depending on the composition. As a result, initially h- Cr_2N followed by body-centred

cubic (bcc) Cr forms. If the Al content of an fcc- $\text{Cr}_{1-x}\text{Al}_x\text{N}$ coating is close to the metastable solubility limit, the phase separation starts at lower temperatures compared to coatings with lower Al content [3, 4]. **Figure 15b** illustrates the decomposition of metastable w- $\text{Cr}_{1-x}\text{Al}_x\text{N}$ coatings. As in the fcc-matrix, w-AlN forms between 1000 and 1300 °C, depending on the composition. However, also fcc-CrN forms and formation of hexagonal- Cr_2N starts later compared to the fcc-matrix [4].

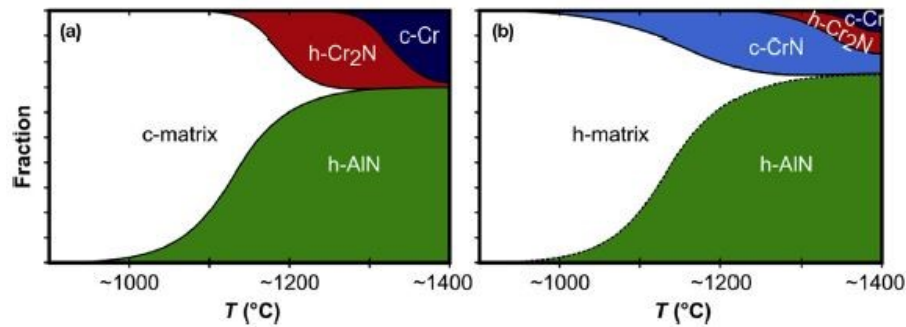


Figure 15: Schematic illustration of the individual phase fractions as a function of annealing temperature for (a) fcc- $\text{Cr}_{1-x}\text{Al}_x\text{N}$, (b) h- $\text{Cr}_{1-x}\text{Al}_x\text{N}$ [4].

The oxidation resistance of $\text{Cr}_{1-x}\text{Al}_x\text{N}$ coatings is improved compared to $\text{Ti}_{1-x}\text{Al}_x\text{N}$. Upon oxidation, $\text{Cr}_{1-x}\text{Al}_x\text{N}$ forms $\alpha\text{-Al}_2\text{O}_3$ and Cr_2O_3 , which are both dense oxide layers. $\alpha\text{-Al}_2\text{O}_3$ and Cr_2O_3 exhibit the smallest growth rates compared to other oxides [3, 4]. $\text{Ti}_{1-x}\text{Al}_x\text{N}$ coatings oxidize at about 700 °C, whereas $\text{Cr}_{1-x}\text{Al}_x\text{N}$ coatings withstand oxidative attack up to 1000 °C. Thus, when the oxidation resistance in the application is of major importance, coatings based on $\text{Cr}_{1-x}\text{Al}_x\text{N}$ are suitable [3, 4].

2.4 Multilayer Coatings

The properties of single layers are often not sufficient for today's demanding applications, which is why multilayer coatings are required. Multilayer coatings consist of two or more individual sublayers with different chemical composition. Nowadays, there are combinations of metal/metal, metal/ceramic and ceramic/ceramic multilayers. Ceramic/ceramic nitride multilayer coatings, e.g. TiN/AlN, TiN/TiAlN or CrN/CrAlN, are the technologically most important multilayer coatings regarding cutting applications [40]. With the progress in the development and utilization of deposition techniques, it has become feasible to create multilayer coatings with varying composition and sublayer thickness. For the deposition of multilayers, two or more single element or alloy targets are required [41]. Shutters, which can

close the individual targets, are needed to achieve a homogeneous layer structure. Another possibility is the preparation of multilayers applying suitable substrate rotation [3, 6]. Thus, sublayer thicknesses as low as a few nm can be realized by PVD [12]. Multilayer coatings allow a wide variety of microstructures in terms of crystallographic orientation, grain size, texture, lattice defects and phase composition [3, 11, 42]. The optimization of the performance of such coatings can be related to atomistic mechanisms at the interface between two crystallographic domains or material systems [1].

The chemical composition and microstructure of the individual layers as well as the sublayer thickness have a strong influence on the properties of multilayer coatings. Furthermore, the combination of alternate ultra-thin layers with higher and lower elastic constants enables to synthesize materials with superior mechanical properties, in comparison to the respective single layers [12]. The combination of several mechanisms, like the Hall-Petch effect, dislocations motion in an alternating strain field and the supermodulus effect are responsible for the improved hardness [40, 42]. Regarding the mechanical properties, Chen *et al.* demonstrated that TiAlN/AlTiN multilayer coatings with a sublayer thickness of ~6 nm and a mixed fcc/w structure exhibit superhardness of up to 57 GPa [29]. Also Li *et al.* reported on an improved hardness of CrAlN/TiAlN multilayer coatings compared to the respective single layers. As the sublayer thickness decreased, the hardness of the coating improved [43]. Furthermore, the toughness of multilayer coatings is commonly higher than that of single layers, due to an inhibited crack propagation. As shown in **Figure 16**, the main mechanisms for the improved toughness are interface delamination, ductile interlayer ligament bridging, crack deflection at the interface among the sublayers and crack tip blunting due to nanoplasticity [40, 44]. The performance of a multilayer coated substrate can be improved with a gradient design, when first an adhesive layer is deposited on the substrate. Some multilayer coatings based on TiAlN and CrAlN have a lower onset temperature of spinodal decomposition compared to the respective single layers due to the presence of internal interfaces and the fact that decomposition starts initially at the interfaces due to surface directed spinodal decomposition (SDSD), which is followed by internal spinodal decomposition. The due to SDSD evolving microstructure contributes to the improved hardness of multilayer coatings [45].

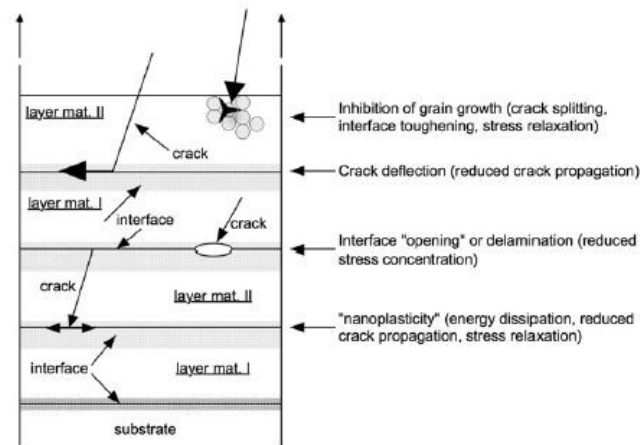


Figure 16: Toughening mechanisms achieved through the application of multilayers [40].

Li *et al.* [43] furthermore state that TiAlN/AlTiN multilayer coatings with a sublayer thickness up to 11 nm have an obvious effect on the SDSA. A disadvantage of multilayer coatings, however, is the mutual solubility of individual layers at elevated temperatures. Heating of such multilayer coatings during application leads to an interdiffusion at the interfaces. This diffusion process can reduce the hardness of multilayer coatings [46, 47].

The oxidation behaviour of multilayer coatings is much more complex compared to single layers due to the altered diffusion properties of the individual sublayers. Therefore, no general statement can be made about the oxidation behaviour of multilayers [47, 48]. In addition to thermal stability and mechanical properties, the multilayered coating architecture is also reported to influence the tribological properties. CrAlN/TiAlN multilayer coatings show excellent performance in tribological application as compared to the properties of the respective single layers [12]. As can be seen in **Figure 17**, the lifetime of CrAlN/TiAlN multilayer coatings in cutting tests is significantly higher than that of the respective single layers [43].

In the last decades, the properties of multilayer coatings were reported in numerous experimental reports [1, 8, 26, 29, 42, 44] and theoretical calculations [12, 49, 50]. With the combination of theoretical approaches and experimental work it is possible to design new wear resistant or functional coatings based on multilayer architectures [2, 3].

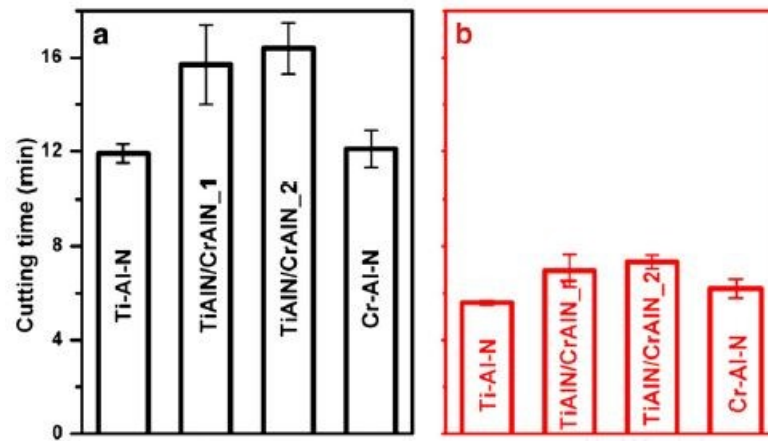


Figure 17: Lifetime of TiAlN, CrAlN single layer and CrAlN/TiAlN multilayer coatings. (a) 160 m/min cutting speed and (b) 200 m/min cutting speed [43].

3 Experimental Methods

3.1 Coating Deposition

A laboratory scale sputtering unit, type AJA International ATC-1800 UHV, located at the Chair of Functional Materials and Materials Systems at the Montanuniversität Leoben, was used for the deposition of the coatings. In **Figure 18** an image of the device is shown. The synthesis of the coatings was performed using four water cooled unbalanced AJA A330 XP UHV magnetrons, arranged in the vacuum chamber as shown in **Figure 19**.

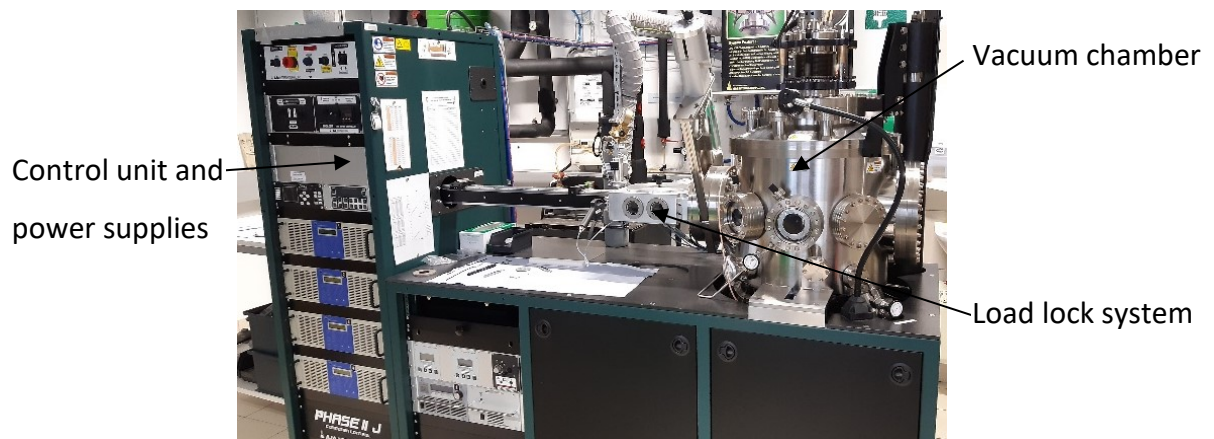


Figure 18: Used sputter deposition device.

Each of the magnetrons was operated by its own power supply. Two of the magnetrons were equipped with planar, circular targets with a Ti/Al ratio of 50/50 and a diameter of 3 inch and a thickness of 0.25 inch. The purity of the targets was 99.5 %. Depending on the series, the following targets with the respective Ti/Al ratios were used for the other two magnetrons: 30/70, 20/80 and in addition Cr/Al 15/85. The targets were positioned on opposing sides and could be covered with a movable shutter, as indicated in **Figure 19**.

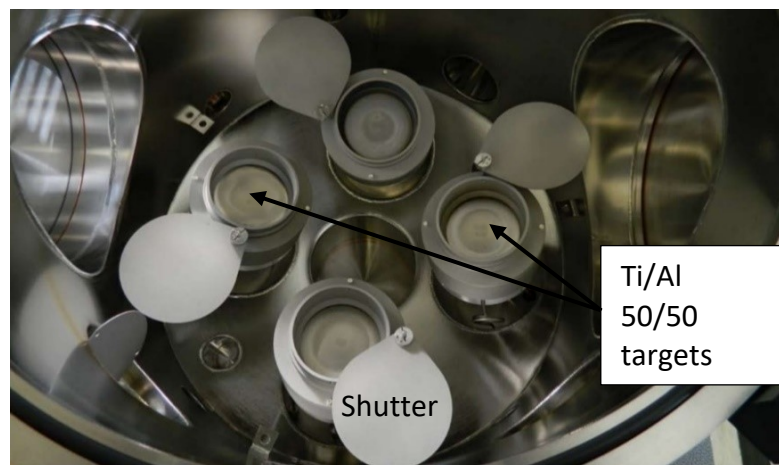


Figure 19: Top view of the vacuum chamber showing the arrangement of the targets.

Cemented carbides with 92 wt.% WC, 6 wt.% Co and 2 wt.% mixed carbides in SNUN geometry were used as substrates. The substrates were ultrasonically pre-cleaned in acetone and ethanol (each for 5 min) and subsequently dried in air before they were mounted on the substrate holder. The sample holder was fixed on a rotary device and was placed in the vacuum chamber with a load lock system.

Before starting the deposition process, the vacuum chamber was pumped to a base pressure $<1 \times 10^{-7}$ mbar. After evacuation, the substrates were heated to the deposition temperature of 350 °C with a heating unit mounted on the back of the sample holder. To remove remaining surface contaminants, the substrates were cleaned by plasma etching in RF mode with a power of 95 W and Ar with a flow rate of 15 sccm. The shutters in front of the targets were closed during the etching process. The Ar pressure in the vacuum chamber was 5×10^{-3} mbar and the duration of the cleaning process was 710 s.

During coating deposition, Ar was regulated to a flow rate of 20 sccm and N₂ to a flow rate of 7.5 sccm. The working pressure in the chamber was 5×10^{-3} mbar. The depositions were performed in bipolarly pulsed DC mode with a power of 400 W, a pulse frequency of 100 kHz and a pulse duration of 1 μs. An RF substrate bias power of 20 W was applied. After deposition, the heating system was turned off automatically and the substrates were cooled down to 100 °C. The individual adjustments for the single layers and multilayer coatings are described in detail in the following two sub-sections.

3.1.1 Single Layer Coatings

Four single layer coatings were deposited to obtain information on the deposition rate, microstructure, crystallographic orientation and mechanical properties. The nomenclature of the single layers (SL) was chosen according to the respective target composition. Thus, SL 50/50, SL 30/70 and SL 20/80 correspond to TiAlN single layers deposited from targets with a Ti/Al ratio of 50/50, 30/70 and 20/80, respectively, and SL CrAl 15/85 corresponds to a single layer deposited from targets with a Cr/Al ratio of 15/85. For SL 50/50, the deposition time was 7000 s, while the duration for the other three single layers was 6500 s. By knowing the deposition time and the measured coating thickness it was possible to calculate the deposition rate and consequently the deposition time for the individual sublayers in the multilayer coatings. The rotation speed of the substrate holder was 60 % of the maximum possible speed. This corresponds to a frequency of 60 revolutions per minute.

3.1.2 Multilayer Coatings

For each multilayer coating system, three different depositions were carried out, aiming for three different sublayer thicknesses, i.e. 3 nm/8 nm, 4 nm/10 nm and 5 nm/12 nm. The first layer of all multilayer coatings was the Ti₅₀Al₅₀N layer.

The nomenclature of the coatings was chosen to include the Ti (or Cr) and Al content in the target and the thickness of the Ti₅₀Al₅₀N layer and the alternating layer. Thus, ML_Ti₃₀Al₇₀_3-8 denotes a TiAlN/AlTiN multilayer, deposited from Ti/Al 50/50 and 30/70 targets, with 3 nm aimed layer thickness of the TiAlN layers and 8 nm aimed layer thickness of the AlTiN layers. The deposition time was two hours, aiming for a coating thickness of ~4 μm. To obtain a homogeneous layer structure of the multilayer coatings, the rotation speed of the substrate holder was elevated to 80 % of the maximum possible speed. This corresponds to a frequency of 80 revolutions per minute.

3.2 Coating Characterization

3.2.1 Coating Thickness

The thickness of the coatings on the cemented carbide was determined with a CSM Calowear test by ball cratering. Subsequently, the sample was investigated with a light optical microscope to measure the inner and outer diameter of the calotte. These diameters were used to calculate the coating thickness. Three calottes were ground in each sample and the mean value and the standard deviation were calculated.

3.2.2 Layer Architecture

In order to verify the layer architecture of the multilayer coatings and to assess the actual sublayer thicknesses, cross-sectional micrographs of exemplary coatings were recorded using a scanning electron microscope (SEM) of type Zeiss Gemini 450. The cross-sections were prepared with a Hitachi IM 4000⁺ ion milling system. Only the single layer coatings and the multilayer coatings within the 3-8 sublayer system were investigated.

3.2.3 Chemical Composition

The chemical composition of the cross-section of the single and exemplarily the 3-8 multilayer coatings on cemented carbide substrates was measured by energy-dispersive X-ray spectroscopy (EDX), using an Oxford Instruments INCA detector on a Zeiss Gemini 450. For quantification built-in sensitivity factors were applied. It has to be noted, that EDX measurements only give a rough estimation of the composition of multilayered coatings.

3.2.4 Microstructure

Information about the crystallographic structure of the investigated coatings was obtained via X-ray diffraction (XRD) using a Bruker D8 Advance diffractometer equipped with Cu-K α radiation. The measurements were performed in grazing incidence geometry within a 2θ range from 25 to 85°. An incidence angle of 2°, a step size of 0.02° and a counting time of 1 s per step were applied. The value for the tube voltage was set to 40 kV and the tube current to 40 mA. The wavelength of Cu-K α radiation is 1.54 Å.

3.2.5 Hardness and Young's modulus

Hardness and Young's modulus of the coatings were measured using a UMIS nanoindenter from Fischer-Cripps Laboratories equipped with a diamond Berkovich tip. The samples were placed in the device for at least 2 hours before the start of the tests to minimize thermal drift. Prior to the experiments, the coating surface was polished by hand to obtain a low and uniform surface roughness. A load from 20 to 10 mN was applied in steps of 0.5 mN. The maximum penetration depth was less than 10 % of the coating thickness to minimize substrate effects. The measurements were evaluated according to the Oliver and Pharr method [51].

4 Results and Discussion

4.1 Single Layer Coatings

4.1.1 Coating Thickness

Table 1 summarizes the thicknesses of the single layer coatings measured by the Calowear test and SEM as well as the deposition rate calculated from the thickness measured with the Calowear test. There is a considerable difference between the thickness as determined by Calowear test and SEM. It is assumed that the reason for this is that the calottes were not ideal circles. Chipping of the coating furthermore decreased the accuracy of the evaluation. As can be seen in **Table 1**, the deposition rate of SL 50/50 is considerably lower than the one of SL 30/70. As the Al content further increases, a plateau is reached, resulting in comparable values of SL 30/70 and SL 20/80. However, the thickness measured by SEM increases and this leads to the assumption that the deposition rate of SL 20/80 calculated from the Calowear test is not correct. Since Al exhibits a higher sputtering yield (Y) compared to Ti, the increasing deposition rate with increasing Al content is in agreement with literature [52]. Exemplary sputtering yields found in literature for Ar ion energies of 400 eV are $Y_{Al} = 0.80$ for Al and $Y_{Ti} = 0.55$ for Ti [53]. The deposition rate of SL CrAl 15/85 exceeds the values of all $Ti_{1-x}Al_xN$ single layer coatings, which can be attributed to the higher sputtering yield of Cr ($Y_{Cr} = 1.11$) compared to Ti [54].

Table 1: Thicknesses measured by Calowear test and SEM as well as the calculated deposition rate of the single layer coatings.

Coating system	Thickness measured with Calowear test [μm]	Thickness measured by SEM [μm]	Deposition rate [nm/s]
SL 50/50	1.5	2.1	0.2
SL 30/70	4.4	4.3	0.7
SL 20/80	4.1	4.6	0.6
SL CrAl 15/85	5.2	4.7	0.8

4.1.2 Chemical Composition

Table 2 shows the chemical composition of the single layer coatings as determined by EDX. All $Ti_{1-x}Al_xN$ single layer coatings exhibit a lower $Ti/(Ti+Al)$ ratio compared to the target. This observation can be attributed to the aforementioned higher sputtering yield of Al compared to Ti [52]. The $Cr/(Cr+Al)$ ratio of SL CrAl 15/85 (0.46) is significantly higher than the one in the target (0.15). Again, this can be ascribed to the sputtering yield, which is higher in case of Cr compared to Al [37]. In addition, selective scattering of the lighter Al atoms might play a role. The nitrogen content for all $Ti_{1-x}Al_xN$ coatings was close to 50 at.%, indicating a stoichiometric composition. For SL CrAl 15/85, the nitrogen content amounts to 35 at.%, which suggests the presence of h- Cr_2N in addition to fcc- $Cr_{1-x}Al_xN$ considering the equilibrium phase diagram of Cr-N [54].

Table 2: Chemical composition of the single layer coatings as determined by EDX.

Coating system	Chemical composition [at.%]				$(Ti,Cr)/((Ti,Cr)+Al)$ ratio
	Ti	Cr	Al	N	
SL 50/50	20	-	30	50	0.40
SL 30/70	12	-	37	51	0.24
SL 20/80	8	-	45	47	0.15
SL CrAl 15/85	-	30	35	35	0.46

4.1.3 Microstructure

As can be seen from the cross-sectional scanning electron micrographs of the coatings in **Figure 20**, all single layer coatings exhibit a fine-grained structure. Some individual grains can be resolved in case of SL 30/70 (**Figure 20b**) and SL 20/80 (**Figure 20c**). This is however not possible in case of SL 50/50 (**Figure 20a**) due to the pronounced tapering from the ion slice and in case of SL CrAl 15/85 (**Figure 20d**) owing to the extremely fine grains. Thus, the micrographs indicate a smaller grain size of SL CrAl 15/85 compared to the $Ti_{1-x}Al_xN$ single layer coatings.

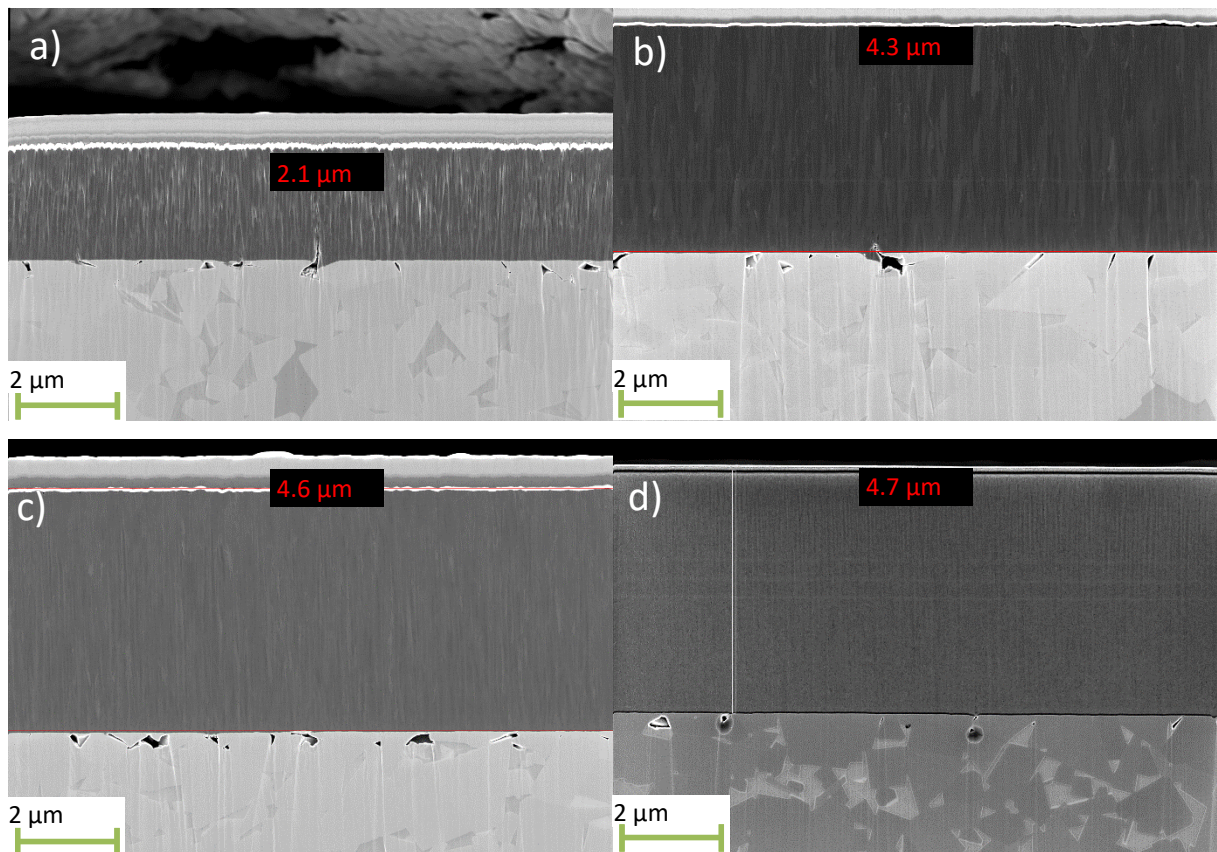


Figure 20: Secondary electron scanning electron micrographs of the cross-sections of a) SL 50/50, b) SL 30/70, c) SL 20/80 and d) SL CrAl 15/85. The measured coating thickness is given as well.

In **Figure 21**, the XRD patterns of the $Ti_{1-x}Al_xN$ single layer coatings are presented. The standard peak positions for the fcc-TiN, fcc-AlN, w-AlN and WC reflections are given as well [55 – 58]. The XRD peaks of SL 50/50 are located in between the standard peak position of fcc-TiN and fcc-AlN, confirming the formation of a fcc-TiAlN solid solution [59]. No indication for the w-AlN phase can be found in the SL 50/50 coating. In addition to fcc-TiAlN peaks, 110 and 102 reflections of the w-structure are present in the SL 30/70 pattern. SL 20/80 exhibits only w peaks. Thus, with increasing Al content, the phase fraction of w-AlTiN increases. The lower density of the w-AlTiN phase is expected to contribute significantly to the increase of the deposition rate for high Al contents reported in **Table 1** [11]. The peaks of w-AlTiN are slightly shifted to lower diffraction angles compared to the standard peak position of w-AlN, indicating the incorporation of Ti atoms into the w-AlN lattice. The full width at half maximum (FWHM) of the XRD reflections increases with increasing Al content. While the 111 fcc-TiAlN peak in SL 50/50 exhibits a FWHM of 0.25° , this value amounts to 0.29° in the SL 20/80. The same trend can be observed for the 100 w-AlTiN peaks, where the FWHM increases from 0.29° in

SL 30/70 to 0.71° in SL 20/80. A larger FWHM correlates with a smaller size of coherently diffracting domains and higher micro-strain [60]. Thus, an increasing Al content in the coatings results in grain refinement and micro-strain intensification.

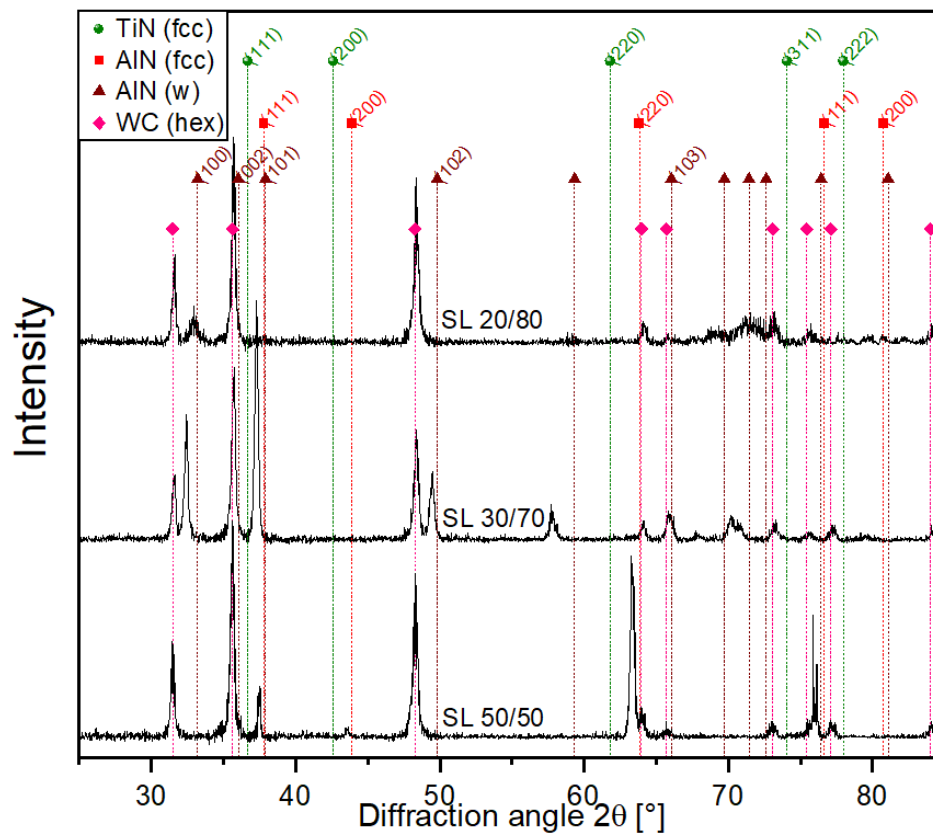


Figure 21: XRD patterns of the $Ti_{1-x}Al_xN$ single layer coatings.

In **Figure 22**, the XRD pattern of SL CrAl 15/85 is shown. The standard peak positions for fcc-CrN, hex-Cr₂N, fcc-AlN, w-AlN and WC stemming from the substrate are given as well [56 – 58, 61, 62]. The detected fcc-CrAlN peaks are located between the standard peak positions of fcc-CrN and fcc-AlN [39]. Thus, as for the TiAlN coatings with low Al content, an fcc-CrAlN solid solution has formed. In addition, reflections stemming from w-Al(Cr)N are detected, although the Cr/(Al+Cr) ratio of 0.45 is significantly lower than the theoretical solubility limit of 0.62 reported in literature [37, 63], which indicates that the deposition parameters need to be further optimized. Moreover, h-Cr₂N reflections are present, which can be attributed to the low N content of 35 at.% (see **Table 2**). The 200 fcc-CrAlN peak exhibits a FWHM of 2.60° . Thus, the FWHM of fcc-CrAlN is significantly larger compared to the one of the $Ti_{1-x}Al_xN$ coatings. Therefore, much smaller grains are present in SL CrAl 15/85, which is in agreement with the impression from the scanning electron micrograph in **Figure 20**.

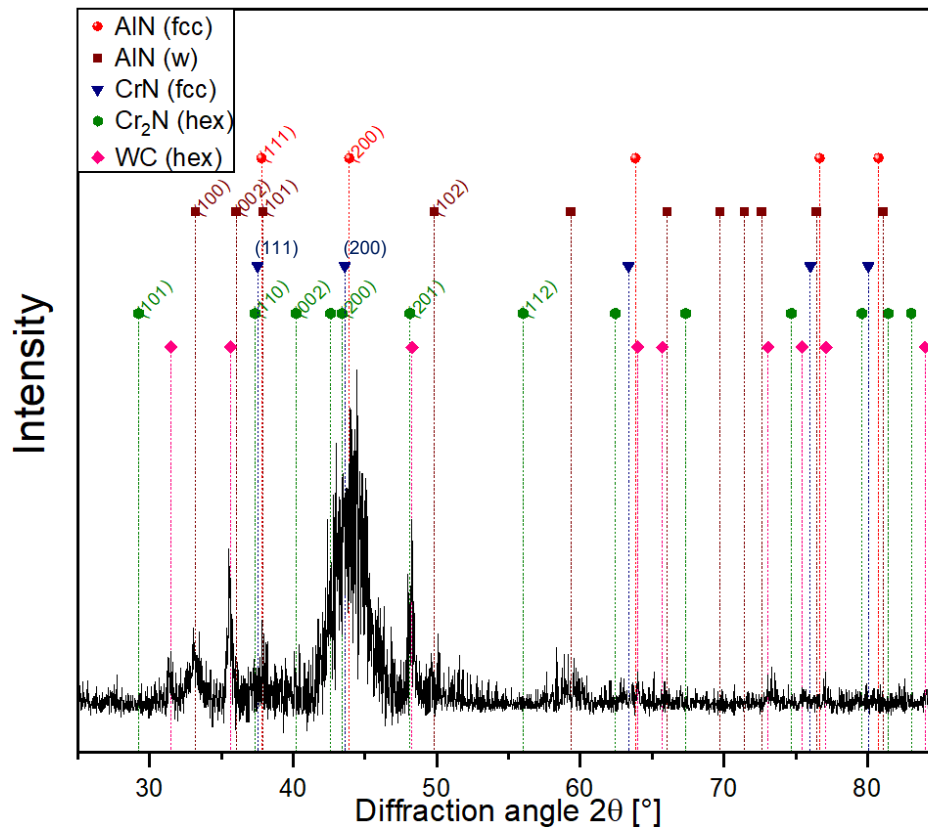


Figure 22: XRD pattern of SL CrAl 15/85.

4.1.4 Mechanical Properties

Figure 23 shows the hardness and the Young's modulus of the four single layer coatings. The error bars depict the calculated standard deviation. SL 50/50 and SL 20/80 have a comparable hardness of ~ 23 GPa. The minimum hardness value of 19.5 ± 1.2 GPa among the $Ti_{1-x}Al_xN$ single layer coatings was determined for SL 30/70. According to PalDey and Deevi [2], the hardness increases with increasing Al content until the metastable solubility limit of the fcc structure is reached. Thus, the here determined trend is in contradiction to literature. It is assumed that the reason for this is that the coatings are not perfectly dense. Thus, optimization of the deposition conditions would be crucial to obtain denser coatings with an improved hardness. The SL CrAl 15/85 exhibits a hardness of 21.0 ± 2.0 GPa and is thus comparable with the value determined for SL 20/80. Among the $Ti_{1-x}Al_xN$ single layer coatings, SL 50/50 exhibits the highest Young's modulus of 432 ± 18 GPa. With increasing Al content, the Young's modulus decreases, resulting in values of ~ 300 GPa for SL 30/70, 20/80 and CrAl 15/85. As mentioned before, the FWHM increases with increasing Al content and therefore the grain size decreases. With smaller grain size, the amount of the grain boundaries

increases. The Young's modulus decreases with increasing amount of grain boundaries, since the grain boundaries represent weak, underdense zones in the material [64].

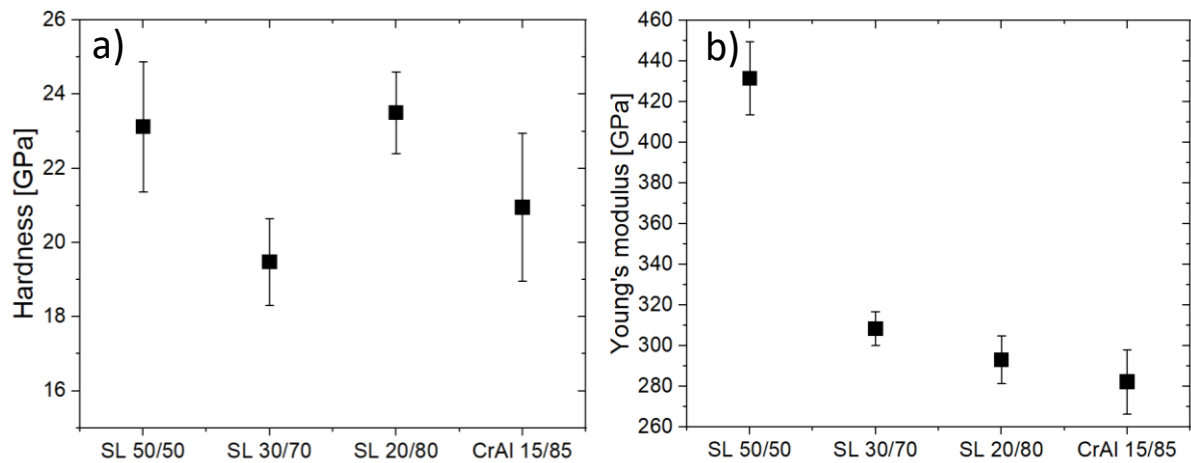


Figure 23: (a) Hardness and (b) Young's modulus of the single layer coatings.

4.2 Multilayer Coatings

4.2.1 Coating Thickness

Table 3 summarizes the thicknesses measured with the Calowear test and the thereof calculated deposition rates as well as the thicknesses determined by SEM of the multilayer coatings. The aimed coating thickness of 4 μm could be achieved for all multilayer coatings. The deposition rates lie between the deposition rates of the respective single layer coatings (see subsection **4.1.1 Coating Thickness**). With increasing sublayer thickness, the deposition rate decreases due to the increased fraction of the $\text{Ti}_{50}\text{Al}_{50}\text{N}$ sublayers, which exhibited a lower deposition rate. In contrast to the single layer coatings, the thicknesses determined with the Calowear test and SEM are in a good agreement with each other. In the following TiAlN layers denote Ti rich, AlTiN layers Al rich layers.

Table 3: Thicknesses measured by the Calowear test and SEM, and calculated deposition rate of the multilayer coatings.

Coating system	Thickness measured with Calowear test [μm]	Thickness measured with SEM [μm]	Deposition rate [nm/s]
ML_Ti ₃₀ Al ₇₀ _3-8	4.3	4.4	0.6
ML_Ti ₂₀ Al ₈₀ _3-8	4.8	4.5	0.7
ML_Cr ₁₅ Al ₈₅ _3-8	5.1	5.0	0.8
ML_Ti ₃₀ Al ₇₀ _4-10	4.0	-	0.6
ML_Ti ₂₀ Al ₈₀ _4-10	4.8	-	0.7
ML_Cr ₁₅ Al ₈₅ _4-10	5.1	-	0.8
ML_Ti ₃₀ Al ₇₀ _5-12	4.3	-	0.6
ML_Ti ₂₀ Al ₈₀ _5-12	4.7	-	0.6
ML_Cr ₁₅ Al ₈₅ _5-12	4.7	-	0.7

4.2.2 Microstructure

In **Figure 24** scanning electron micrographs showing an overview of the multilayer coatings within the 3-8 sublayer system are exemplarily presented. As for the single layer coatings, the multilayer coatings exhibit a fine-grained structure. Due to the higher mass contrast of the CrAlN/TiAlN coatings compared to TiAlN/AlTiN, the individual CrAlN and TiAlN sublayers can be differentiated in **Figure 24c** already at this rather low magnification. Brighter layers correspond to the CrAlN layers, dark ones to the TiAlN layers. At the given magnification, it is not possible to resolve the individual layers in the TiAlN/AlTiN multilayers.

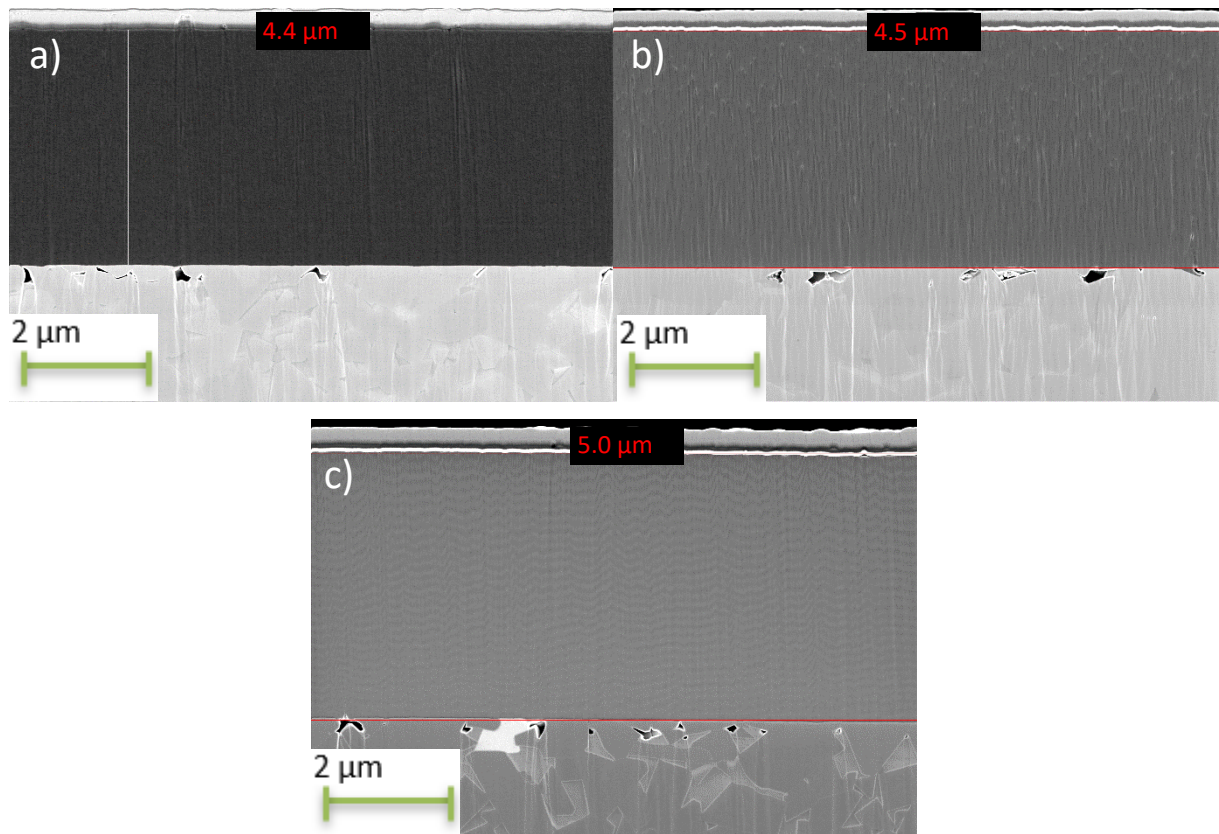


Figure 24: Secondary electron scanning electron micrographs of the (a) ML_Ti₃₀Al₇₀_3-8, (b) ML_Ti₂₀Al₈₀_3-8 and (c) ML_Cr₁₅Al₈₅_3-8 multilayer coating. The measured coating thickness is given as well.

In order to be able to resolve the layers also in the TiAlN/AlTiN multilayer coatings, scanning electron micrographs, shown in **Figure 25**, were recorded at a higher magnification. The individual layers can be resolved in case of ML_Ti₂₀Al₈₀_3-8 (**Figure 25b**). Bright layers correspond to TiAlN layers, dark ones to AlTiN layers. Also with the higher magnification applied, it is hardly possible to resolve the individual layers of ML_Ti₃₀Al₇₀_3-8. It is assumed that the mass contrast between the individual layers of ML_Ti₃₀Al₇₀_3-8 is too low to unambiguously resolve the layers by means of SEM.

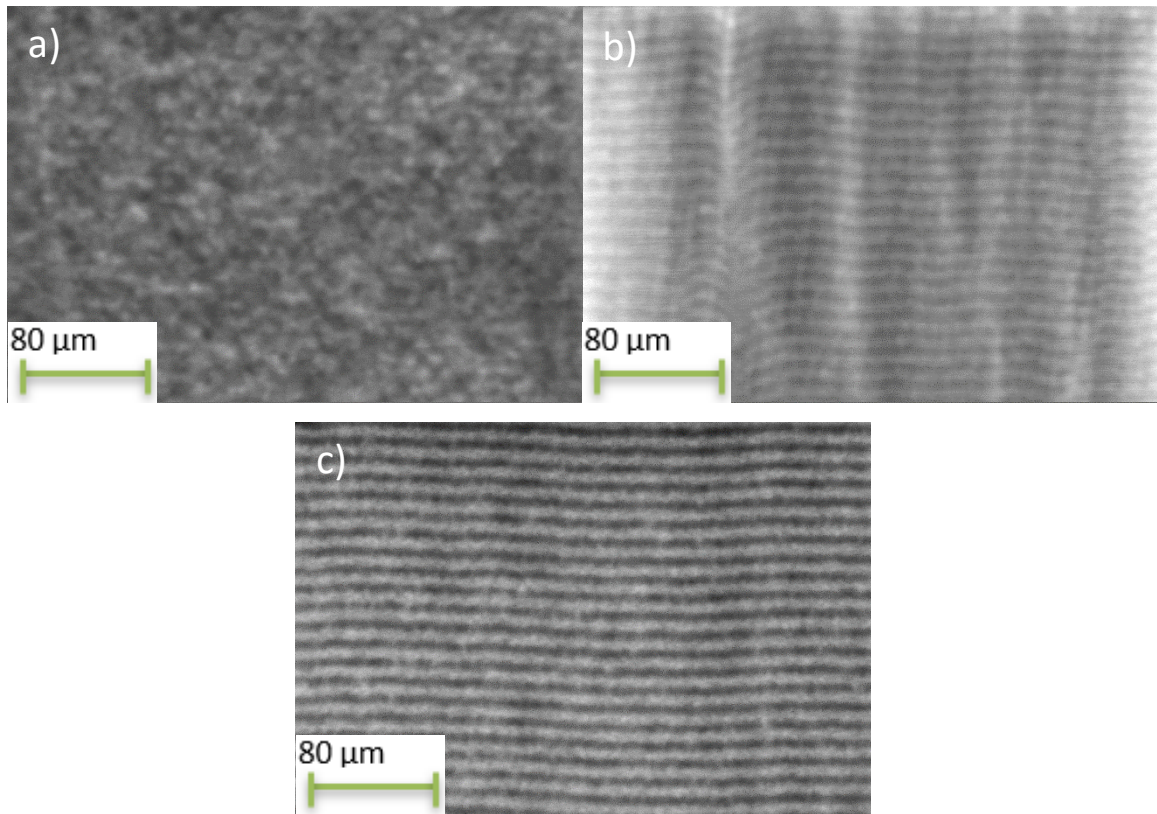


Figure 25: Secondary electron scanning electron micrographs of the a) ML_Ti₃₀Al₇₀_3-8, (b) ML_Ti₂₀Al₈₀_3-8 and (c) ML_Cr₁₅Al₈₅_3-8 multilayer coatings recorded at higher magnification.

From the micrographs shown in Fig. 25, the respective sublayer thicknesses were determined.

Table 4 compares the aimed and real sublayer thickness of the multilayer coatings. The resolution of the used SEM was too low to determine the sublayer thicknesses of the ML_Ti₃₀Al₇₀. The measured thickness of the Ti₂₀Al₈₀N sublayers and the Cr₁₅Al₈₅N sublayers is in reasonable agreement with the aimed dimensions. The actual thicknesses of the Ti₅₀Al₅₀N sublayers determined for the 3-8 multilayer coatings were, however, significantly higher than the aimed thickness. It is assumed that the inaccurate estimation of the deposition rate of the Ti₅₀Al₅₀N single layer from the Calowear test is the reason for the higher thickness of these layers. Since the sublayer thicknesses of the ML_Ti₃₀Al₇₀ could not be measured, no values are given in **Table 4** for this coating system.

Table 4: Aimed sublayer thickness and actual sublayer thickness of the multilayer coatings.

Coating system	Aimed sublayer thickness [nm]		Actual sublayer thickness [nm]	
	Ti ₅₀ Al ₅₀ N	Alternating layer	Ti ₅₀ Al ₅₀ N	Alternating layer
ML_Ti ₂₀ Al ₈₀ _3-8	3	8	7.6 ± 0.7	10.1 ± 0.9
ML_Cr ₁₅ Al ₈₅ _3-8	3	8	5.0 ± 0.3	11.0 ± 1.0

In the following, the results of the XRD investigations of the multilayer coatings with the same composition, but varying sublayer thickness are compared. In **Figure 26**, the XRD patterns of the ML_Ti₃₀Al₇₀ coatings are presented. These multilayer coatings exhibit a fcc-TiAlN solid solution. Thus, the peaks are located between the standard peak positions for fcc-TiN and fcc-AlN [55, 56]. In contrast to SL 30/70, no w-AlN reflections are detected. This observation indicates that the Ti₅₀Al₅₀N layers stabilize the fcc-structure in the higher Al containing layers. The FWHM of the 200 reflection decreases with increasing sublayer thickness from 1.38° in the 3-8 coating to 1.23° in the 5-12 coating. Therefore, a reduction of the sub-layer thickness results in grain refinement and intensification of the micro-strain, which has also been reported by other authors [65].

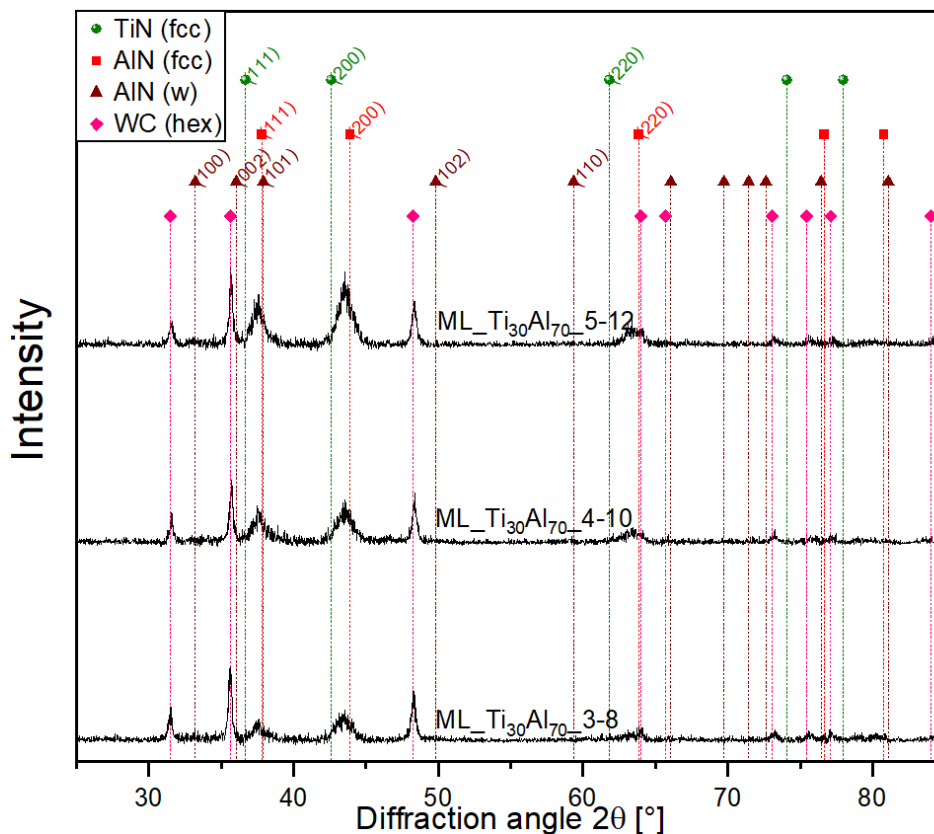


Figure 26: XRD patterns of the ML_Ti₃₀Al₇₀ coatings.

Figure 27 shows the XRD patterns of the ML_Ti₂₀Al₈₀ coatings, which have a similar crystallographic structure as the ML_Ti₃₀Al₇₀ coatings, but also exhibit small 100 w-AlTiN reflections. However, in contrast to SL 20/80, the fcc-TiAlN phase is still present in case of the ML_Ti₂₀Al₈₀ coatings. Thus, also for this coating, the Ti₅₀Al₅₀N sublayer allowed a stabilization of the fcc-structure. Peak intensities and FWHM are comparable for all ML_Ti₂₀Al₈₀ coatings, irrespective of the sublayer thickness.

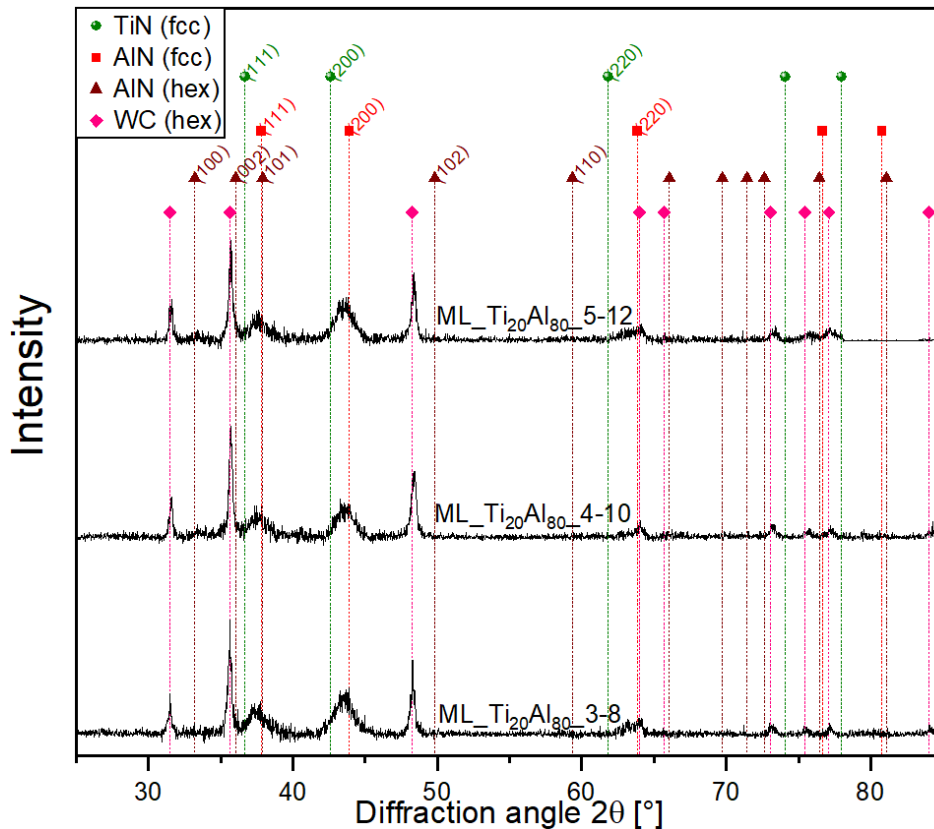


Figure 27: XRD patterns of the ML_{Ti₂₀Al₈₀} coatings.

In **Figure 28**, the XRD patterns of the ML_{Cr₁₅Al₈₅} coatings are shown. The reflections are located between the standard peak positions of fcc-CrN and fcc-AlN, confirming the formation of the fcc-CrAlN solid solution. At $2\theta \sim 37.5^\circ$ it is not possible to distinguish whether w-AlTiN or fcc-TiAlN is present. In addition, a 211 reflection attributed to h-Cr₂N is observed. The intensities of the peaks slightly increase with increasing sublayer thickness. As in the ML_{Ti₃₀Al₇₀} coatings, the FWHM of the 200 fcc-CrAlN peak decreases with increasing sublayer thickness from 2.41° in the 3-8 coating to 1.70° in the 5-12 coating. Thus, a lower sublayer thickness induces a smaller domain size and increased micro-strain. Although a stabilization of the fcc regime can be also suggested for the ML_{Cr₁₅Al₈₅} coatings, the effect seems to be less pronounced compared to the TiAlN/AlTiN coatings.

coating is lower than the theoretical ratio. The nitrogen content for all TiAlN/AlTiN coatings was approximately 43 at.% and thus, clearly understoichiometric. For the ML_Cr₁₅Al₈₅_3-8 coating, the nitrogen content was 31 at.%. Thus, all multilayer coatings exhibit a lower nitrogen content than the corresponding single layer coatings.

Table 5: Comparison of the theoretical metal fraction (**Equation 4.1**) with the measured chemical compositions of the multilayer coatings within the 3-8 sublayer system.

Coating system	Theoretical (Ti,Cr)/((Ti,Cr)+Al) ratio	Composition as determined by EDX [at.%]				Actual (Ti,Cr)/((Ti,Cr)+Al) ratio
		Ti	Cr	Al	N	
ML_Ti ₃₀ Al ₇₀ _3-8	0.28*	19	-	38	43	0.33
ML_Ti ₂₀ Al ₈₀ _3-8	0.26	16	-	41	43	0.28
ML_Cr ₁₅ Al ₈₅ _3-8	0.36	10	18	41	31	0.31

* theoretical ratio was estimated with the aimed sublayer thickness.

4.2.4 Mechanical Properties

As can be seen in **Figure 29**, the mechanical properties of the investigated coatings are not affected by the sublayer thickness to a large extent. For each composition system, the values of the hardness and Young's modulus basically spread within the standard deviation for the different sublayer thicknesses. The chemical and consequently the phase composition of the coating, however, has a significant influence on the mechanical properties. The ML Ti₃₀Al₇₀N coatings exhibit a hardness of $\sim 23 \pm 1.1$ GPa and a Young's modulus of $\sim 350 \pm 14$ GPa, making them the hardest and stiffest variation among the investigated multilayers. The lower hardness ($\sim 20 \pm 1.1$ GPa) and Young's modulus ($\sim 300 \pm 13$ GPa) of the ML_Ti₂₀Al₈₀N coatings is attributed to the presence of the w-structure, which is reported to deteriorate the mechanical properties [29]. The fact that SL 20/80 exhibits a higher hardness than the corresponding multilayer coatings is contradictory to theoretical considerations. According to Wang *et al.* [40], the application of a multi-layered coating architecture improves the hardness due to prevention of dislocation movement. It is suggested that the reason for the here observed trend is that the coating is not fully dense. This assumption applies as well to the CrAlN/TiAlN multilayer coating. The lowest hardness and Young's modulus values of ~ 17 GPa ± 0.7 and 290 ± 8 GPa, respectively, are obtained for the ML_Cr₁₅Al₈₅ coatings. In

conclusion, it should be mentioned that the absolute values and trends of the mechanical properties of the coatings only partly agree with data from the literature [29, 43]. This fact highlights again the necessity to further optimize the deposition parameters.

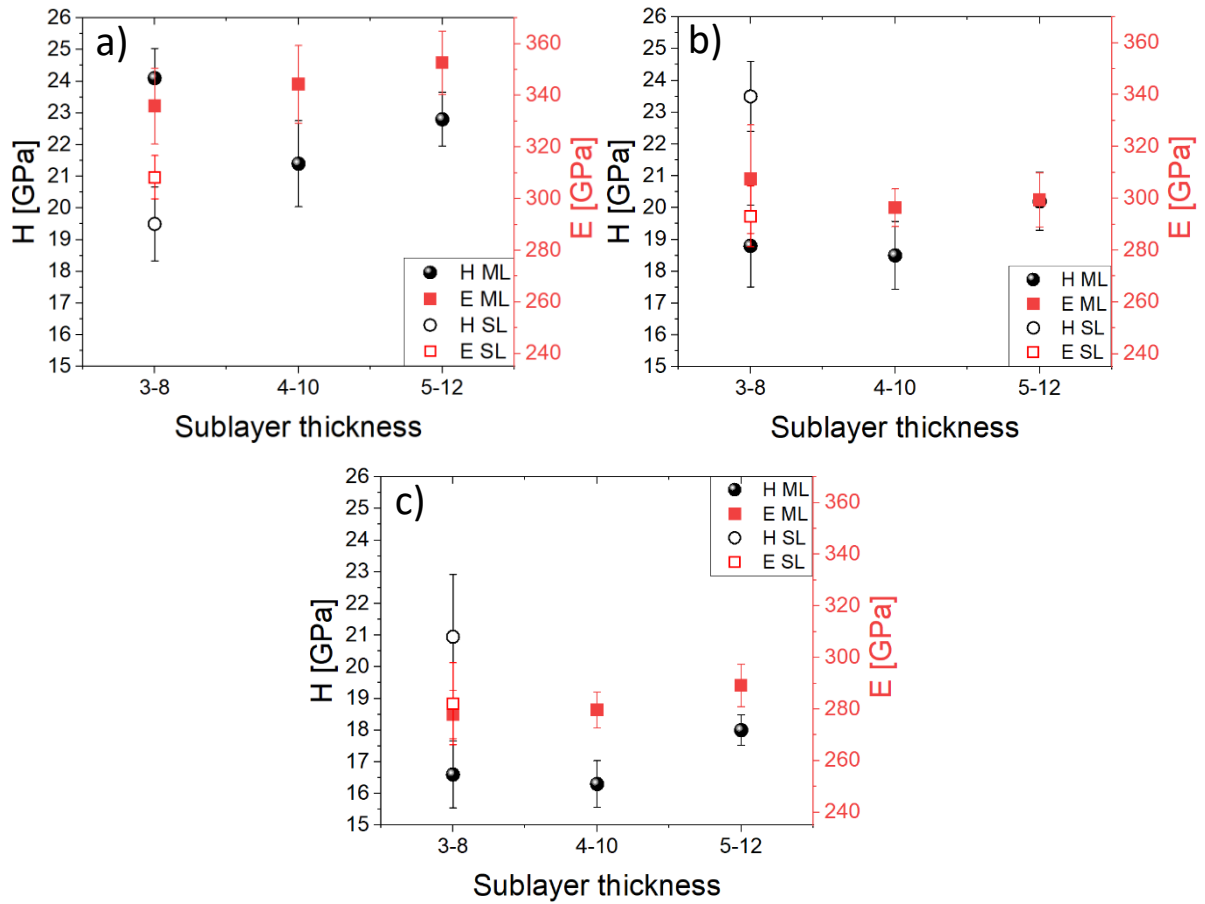


Figure 29: Hardness H and Young's modulus E of the (a) ML_Ti₃₀Al₇₀, (b) ML_Ti₂₀Al₈₀ and (c) ML_Cr₁₅Al₈₅ multilayer coatings over the sublayer thicknesses.

5 Summary and Conclusion

The aim of this thesis was to synthesize TiAlN/AlTiN and CrAlN/TiAlN multilayer coatings as well as the corresponding $Ti_{1-x}Al_xN$ and $Cr_{1-x}Al_xN$ single layers and to investigate their microstructure and mechanical properties. Four single layer coatings and nine multilayer coatings with different (Ti, Cr)/Al ratio and different sublayer thickness were deposited by reactive magnetron sputtering in a laboratory sputtering unit. The deposited coatings were investigated by Calowear tests, X-ray diffraction and nanoindentation. In addition, all single layer coatings and selected multilayer coatings were investigated by scanning electron microscopy and energy-dispersive X-ray spectroscopy.

It could be shown that magnetron sputtering is a suitable technique for the deposition of TiAlN/AlTiN and CrAlN/TiAlN multilayer coatings with sublayer thickness down to ~5 nm. All coatings exhibited a polycrystalline fine-grained structure. The XRD pattern of SL 50/50 showed a single-phase fcc-TiAlN structure. SL 30/70 exhibited a dual-phase fcc/w structure and SL 20/80 was pure w-AlTiN. Thus, with higher Al content the amount of w-AlTiN increased in the single layers. The SL CrAl 15/85 exhibited a dual-phase fcc/w structure. All ML_Ti₃₀Al₇₀ coatings were characterized by a single-phase fcc-TiAlN structure, independent of the sublayer thickness, while the ML_Ti₂₀Al₈₀ coatings showed minor w-AlTiN reflections. However, considering the purely wurtzitic SL 20/80, it can be concluded that the application of the multilayered coating architecture stabilizes the fcc-structure. The ML_Cr₁₅Al₈₅ exhibited a dual-phase fcc/w structure, comparable to the single layer.

Within the TiAlN single layer coatings, the hardness decreased from 23.1 ± 1.8 GPa in SL 50/50 to 19.5 ± 1.2 GPa in SL 30/70, but increased to 23.5 ± 1.1 GPa for the SL 20/80 again. The hardness of SL CrAl 15/85 was 20.9 ± 2 GPa. With increasing Al content, the Young's modulus of the deposited coatings decreased from 432 ± 18 GPa in SL 50/50 to 293 ± 12 GPa in SL 20/80. The Young's modulus of SL CrAl 15/85 was 282 ± 16 GPa. No significant influence of the sublayer thickness on the mechanical properties was observed. The results of the nanoindentation experiments of the coatings were in discrepancy with literature, regarding both the absolute values and the trend. This fact is attributed to a low density of the coating and a non-optimized structure.

Summarizing, it could be shown that the application of a multilayered coating architecture allows to stabilize the fcc-structure especially in TiAlN/AlTiN coatings. However, further

optimization of the deposition conditions would be crucial to obtain coatings with improved mechanical properties. In order to assess the applicability of the deposited coatings for cutting applications, further investigations on thermal stability, wear behaviour and adhesion should be done. Coatings with a modified layer architecture or deposition parameters might result in denser coatings with a higher hardness compared to the coatings in this thesis.

References

- [1] C.M. Koller, R. Hollerweger, C. Sabitzer, R. Rachbauer, S. Kolozsvári, J. Paulitsch, P.H. Mayrhofer. Thermal stability and oxidation resistance of arc evaporated TiAlN, TaAlN, TiAlTaN, and TiAlN/TaAlN coatings. *Surface and Coatings Technology*, 259, 599–607, 2014.
- [2] S. PalDey, S.C. Deevi. Single layer and multilayer wear resistant coatings of (Ti, Al)N: A review. *Materials Science and Engineering*, 342, 58–79, 2003.
- [3] C. Mitterer. PVD and CVD Hard Coatings. *Comprehensive Hard Materials*, 449–467, 2014.
- [4] P.H. Mayrhofer, R. Rachbauer, D. Holec, F. Rovere, and J.M. Schneider. Protective transition metal nitride coatings. pages 355–388, 2014.
- [5] P.H. Mayrhofer, R. Rachbauer, D. Holec, F. Rovere, J.M. Schneider. Protective Transition Metal Nitride Coatings. *Comprehensive Materials Processing*, 355–388, 2014.
- [6] W. D. Sproul. Physical vapor deposition tool coatings. *Surface and Coatings Technology*, 81, 1–7, 1996.
- [7] D. Holec, L. Zhou, R. Rachbauer, P. H. Mayrhofer. Alloying-related trends from first principles: An application to the Ti-Al-X-N system. *Journal of Applied Physics*, 113, 113510, 2013.
- [8] M. Kathrein, C. Michotte, M. Penoy, P. Polcik, C. Mitterer. Multifunctional multi-component PVD coatings for cutting tools. *Surface and Coatings Technology*, 200, 1867–1871, 2005.
- [9] R. Rachbauer, J. Gengler, A. Voevodin, K. Resch, P. H. Mayrhofer. Temperature driven evolution of thermal, electrical, and optical properties of Ti-Al-N coatings. *Acta Materialia*, 60, 2091–2096, 2012.
- [10] I. Park, D. S. Kang, J. Moore, S. C. Kwon, J. J. Rha, K. H. Kim. Microstructures, mechanical properties, and tribological behaviors of Cr-Al-N, Cr-Si-N, and Cr-Al-Si-N coatings by a hybrid coating system. *Surface and Coatings Technology*, 201, 5223–5227, 2007.
- [11] P. H. Mayrhofer, C. Mitterer, L. Hultman, H. Clemens. Microstructural design of hard coatings. *Progress in Materials Science*, 51, 1032–1114, 2006.
- [12] V. Chawla, D. Holec, P. H. Mayrhofer. The effect of interlayer composition and thickness on the stabilization of cubic AlN in AlN/Ti-Al-N superlattices. *Thin Solid Films*, 565, 94–100, 2014.
- [13] P. Martin. *Handbook of deposition technologies for films and coatings: science, applications and technology*. Elsevier, Amsterdam Boston, 2010.

- [14] D. M. Mattox. Handbook of physical vapor deposition (PVD) processing. William Andrew Elsevier Science distributor, Norwich, N.Y. Oxford, 2010.
- [15] V. Zin, E. Miorin, S. M. Deambrosis, F. Montagner, M. Fabrizio. Mechanical properties and tribological behaviour of Mo-N coatings deposited via high power impulse magnetron sputtering on temperature sensitive substrates. *Tribology International*, 119, 372–380, 2018.
- [16] Z. Han, J. Tian, Q. Lai, X. Yu, G. Li. Effect of N₂ partial pressure on the microstructure and mechanical properties of magnetron sputtered CrN_x films. *Surface and Coatings Technology*, 162, 189–193, 2003.
- [17] R. A. Haefer. Oberflächen- und Dünnschicht-Technologie. Teil I, Beschichtungen von Oberflächen, Springer Verlag, Berlin, 1987.
- [18] P.J Kelly and R.D Arnell. Magnetron sputtering: a review of recent developments and applications. *Vacuum*, 56, 159–172, 2000.
- [19] B. A. Movchan, A. V. Demchishin. Structure and properties of thick condensates of nickel, titanium, tungsten, aluminum oxides, and zirconium dioxide in vacuum. *Phys.Met. Metallogr.*, 28, 653–660, 1969.
- [20] John A. Thornton. Influence of apparatus geometry and deposition conditions on the structure and topography of thick sputtered coatings. *Journal of Vacuum Science and Technology*, 11(4), 666–670, 1974.
- [21] R. Messier, A. P. Giri, and R. A. Roy. Revised structure zone model for thin film physical structure. *Journal of Vacuum Science & Technology A*, 2(2), 500–503, 1984.
- [22] A. Anders. A structure zone diagram including plasma-based deposition and ion etching. *Thin Solid Films*, 518, 4087–4090, 2010.
- [23] H. Holleck. Material selection for hard coatings. *Journal of Vacuum Science & Technology A*, 4(6), 2661–2669, 1986.
- [24] K. Bobzin, N. Bagcivan, P. Immich, C. Pinero, N. Goebbels, A. Krämer. PVD eine Erfolgsgeschichte mit Zukunft. *Materialwissenschaft und Werkstofftechnik*, 39, 5–12, 2008.
- [25] Li. Zhou. First-principles studies of CrN-based materials. PhD Thesis, TU Wien, 2015.
- [26] M. Popovic, M. Novakovic, A. Traverse, K. Zhang, N. Bibic, H. Hofsäss, K.P. Lieb. Modifications of reactively sputtered titanium nitride films by argon and vanadium ion implantation: Microstructural and opto-electric properties. *Thin Solid Films*, 531, 189–196, 2013.
- [27] F. Uny, E. Blanquet, F. Schuster, Frédéric Sanchette. Ti-Al-N-Based Hard Coatings: Thermodynamical Background, CVD Deposition, and Properties. A Review. *Coatings and Thin-Film Technologies*, 2019.

- [28] P. H. Mayrhofer, D. Music, and J. M. Schneider. Influence of the Al distribution on the structure, elastic properties, and phase stability of supersaturated $Ti_{1-x}Al_xN$. *Journal of Applied Physics*, 100, 094906, 2006.
- [29] L. Chen, Y. X. Xu, Y. Du, Y. Liu. Effect of bilayer period on structure, mechanical and thermal properties of TiAlN/AlTiN multilayer coatings. *Thin Solid Films*, 592, 207–214, 2015.
- [30] R. Rachbauer. Comparative microstructural investigations of Ti-Al-N thin films alloyed with Y or Nb. Master's thesis, Montanuniversität Leoben, 2008.
- [31] E O Hall. The Deformation and Ageing of Mild Steel: III Discussion of Results. *Proceedings of the Physical Society. Section B*, 64, 747–753, 1951.
- [32] N.J. Petch. The cleavage strength of polycrystals. *J. Iron Steel Inst. London*, 173, 25–28, 1953.
- [33] P. H. Mayrhofer, Anders H., L. Karlsson, J. Sjölen, T. Larsson, C. Mitterer, L. Hultman. Self-organized nanostructures in the Ti-Al-N system. *Applied Physics Letters*, 83, 2049–2051, 2003.
- [34] L. Chen, J. Paulitsch, Y. Du, P. H. Mayrhofer. Thermal stability and oxidation resistance of Ti-Al-N coatings. *Surface and Coatings Technology*, 206, 2954–2960, 2012.
- [35] C. Jarms, H.-R. Stock, P. Mayr. Mechanical properties, structure and oxidation behaviour of $Ti_{1-x}Al_xN$ -hard coatings deposited by pulsed d.c. plasma-assisted chemical vapour deposition (PACVD). *Surface and Coatings Technology*, 108-109, 206–210, 1998.
- [36] J. Todt, J. Zalesak, R. Daniel, R. Pitonak, A. Köpf, R. Weißenbacher, B. Sartory, C. Mitterer, J. Keckes. Al-rich cubic $Al_{0.8}Ti_{0.2}N$ coating with self-organized nano-lamellar microstructure: Thermal and mechanical properties. *Surface and Coatings Technology*, 291, 89–93, 2016.
- [37] T. Weirather, C. Czettel, P. Polcik, M. Kathrein, C. Mitterer. Industrial-scale sputter deposition of $Cr_{1-x}Al_xN$ coatings with $0.21 \leq x \leq 0.74$ from segmented targets. *Surface and Coatings Technology*, 232, 303–310, 2013.
- [38] M. Mühlbachler. Influence of Fe impurities on structure and properties of AlCrN films grown by cathodic arc evaporation. Master's thesis, Montanuniversität Leoben, 2011.
- [39] H. Hasegawa, M. Kawate, T. Suzuki. Effects of Al contents on microstructures of $Cr_{1-x}Al_xN$ and $Zr_{1-x}Al_xN$ films synthesized by cathodic arc method. *Surface and Coatings Technology*, 200, 2409–2413, 2005.
- [40] Y. X. Wang, S. Zhang. Toward hard yet tough ceramic coatings. *Surface and Coatings Technology*, 258, 1–16, 2014.

- [41] C.-T. Huang, J.-G. Duh. Deposition of (Ti,Al)N films on A2 tool steel by reactive r.f. magnetron sputtering. *Surface and Coatings Technology*, 71, 259–266, 1995.
- [42] S. H. Yao, Y. L. Su, W. H. Kao, K. W. Cheng. TiN-AlN nanomultilayer films for microdrilling and machining. *Surface Engineering*, 21, 307–314, 2005.
- [43] P. Li, L. Chen, S. Q. Wang, B. Yang, Y. Du, J. Li, M. J. Wu. Microstructure, mechanical and thermal properties of TiAlN/CrAlN multilayer coatings. *International Journal of Refractory Metals and Hard Materials*, 40, 51–57, 2013.
- [44] R. K. Upadhyay, L. A. Kumaraswamidhas. Investigation of monolayer-multilayer PVD nitride coating. *Surface Engineering*, 31, 123–133, 2014.
- [45] A. Knutsson, I. C. Schramm, K. A. Grönhagen, F. Mücklich, M. Odén. Surface directed spinodal decomposition at TiAlN/TiN interfaces. *Journal of Applied Physics*, 113, 114305, 2013.
- [46] A. O. Volkhonskii, I. V. Blinkov, Yu. V. Levinsky, E. A. Skryleva. Evaluation of Thermal Stability of Multilayered Nanostructured Coatings Based on Analysis of Diffusion Mobility of Components of the Layers. *Russian Journal of Non-Ferrous Metals*, 58, 678–683, 2017.
- [47] H. C. Barshilia, A. Jain, K.S. Rajam. Structure, hardness and thermal stability of nanolayered TiN/CrN multilayer coatings. *Vacuum*, 72, 241–248, 2003.
- [48] P. Panjan, B. Navinšek, A. Cvelbar, A. Zalar, J. Vlcek. High-temperature oxidation of TiN/CrN multilayers reactively sputtered at low temperatures. *Surface and Coatings Technology*, 98, 1497–1502, 1998.
- [49] E. Bemporad, M. Sebastiani, F. Casadei, F. Carassiti. Modelling, production and characterisation of duplex coatings (HVOF and PVD) on Ti-6Al-4V substrate for specific mechanical applications. *Surface and Coatings Technology*, 201, 7652–7662, 2007.
- [50] R. Ali, M. Sebastiani, E. Bemporad. Influence of Ti-TiN multilayer PVD-coatings design on residual stresses and adhesion. *Materials & Design*, 75, 47–56, 2015.
- [51] W.C. Oliver, G.M. Pharr. An improved technique for determining hardness and elastic modulus using load and displacement sensing indentation experiments. *Journal of Materials Research*, 7, 1564–1583, 1992.
- [52] K. Kutschej, P.H. Mayrhofer, M. Kathrein, P. Polcik, R. Tessedri, C. Mitterer. Structure, mechanical and tribological properties of sputtered $Ti_{1-x}Al_xN$ coatings with $0.5 \leq x \leq 0.75$. *Surface and Coatings Technology*, 200, 2358–2365, 2005.
- [53] F. Sanchette, T. Czerwiec, A. Billard, C. Frantz. Sputtering of Al-Cr and Al-Ti composite targets in pure Ar and in reactive Ar-N₂ plasmas. *Surface and Coatings Technology*, 96, 184–190, 1997.

- [54] P.B Barna, M. Adamik, J. Lábár, L. Kövér, J. Tóth, A. Dévényi, R. Manaila. Formation of polycrystalline and microcrystalline composite thin films by codeposition and surface chemical reaction. *Surface and Coatings Technology*, 125, 147–150, 2000.
- [55] Int. Cent. Diffr. Data, Pdf-2/Release 2007, card number 00-038-1420.
- [56] Int. Cent. Diffr. Data, Pdf-2/Release 2007, card number 00-025-1495.
- [57] Int. Cent. Diffr. Data, Pdf-2/Release 2007, card number 00-025-1133.
- [58] Int. Cent. Diffr. Data, Pdf-2/Release 2007, card number 00-025-1047.
- [59] A. Kimura, H. Hasegawa, K. Yamada, T. Suzuki. Effects of Al content on hardness, lattice parameter and microstructure of $Ti_{1-x}Al_xN$ films. *Surface and Coatings Technology*, 120-121, 438–441, 1999.
- [60] A. Hörling, L. Hultman, M. Odén, J. Sjöln, L. Karlsson. Mechanical properties and machining performance of $Ti_{1-x}Al_xN$ -coated cutting tools. *Surface and Coatings Technology*, 191, 384–392, 2005.
- [61] Int. Cent. Diffr. Data, Pdf-2/Release 2007, card number 03-065-2899.
- [62] Int. Cent. Diffr. Data, Pdf-2/Release 2007, card number 00-035-0803.
- [63] B. Großmann, N. Schalk, C. Czettl, M. Pohler, C. Mitterer. Phase composition and thermal stability of arc evaporated $Ti_{1-x}Al_xN$ hard coatings with $0.4 \leq x \leq 0.67$. *Surface and Coatings Technology*, 309, 687–693, 2017.
- [64] P. H. Mayrhofer. *Materials Science Aspects of Nanocrystalline PVD Hard Coatings*. PhD Thesis, Montanuniversität Leoben, 2001.
- [65] C. Kainz, N. Schalk, M. Tkadletz, C. Mitterer, C. Czettl. Microstructure and mechanical properties of CVD TiN/TiBN multilayer coatings. *Surface and Coatings Technology*, 370, 311–319, 2019.